GBT memo series **GBT memo 325**

Final Commissioning Report for the Green Bank Telescope 0.7–4 GHz Ultrawideband Receiver

Ryan S. Lynch, Joe Brandt, Jonah Bauserman, Ray Creager, Philip Doolittle, Dennis Egan, Priscilla Grimes, Matthew Harrison, Laura Jensen Nathaniel Langston, Laura Leyzorek, Paul Marganian, David Monasterio, Kirstin Morin, JD Nelson, Scott Ransom, Patrick Schaffner, Bob Simon, Bob Simmons, Harry Sipe, Nathaniel D. Sizemore, Art Symmes, Galen Watts, Steve White

Date: June 26, 2026
Keys: ultrawideband receiver, prime focus, focus tracking model, polarization, pulsars, methylidyne (CH), Hα recombination lines, neutral hydrogen (HI)

Abstract

The ultrawideband receiver (UWBR) is a new front-end instrument for the Green Bank Telescope (GBT). It is installed at the GBT's prime focus and is sensitive to dual linear polarizations with an instantaneous bandwidth of 3.3 GHz, covering 0.7–4 GHz. UWBR is optimized for the study of gravitational waves (GWs) and other areas of fundamental physics through high-precision pulsar timing. It's wide instantaneous bandwidth is also valuable for studying other aspects of pulsar astronomy, fast radio bursts (FRBs), radio magnetars, and the interstellar medium (through molecular line emission).

The science requirements for UWBR are a "cold sky" system temperature of 30 K (this includes all instrumental and sky contributions, except for the Galactic background) and a total aperture efficiency of 0.7 at frequencies < 2.8 GHz, decreasing to 0.5 at 4 GHz. This corresponds to a system equivalent flux density $\mathrm{SEFD} = T_{\mathrm{sys}}/G = 15\text{–}21.3$ Jy. We expect a receiver with this SEFD to improve the RMS of long-term, high-precision pulsar timing residuals by approximately a factor of two.

UWBR has gone though a number of modifications in an attempt to meet these goals. It was installed on the GBT in its final configuration for commissioning observations in October and November 2025. After excising frequencies contaminated by radio frequency interference (RFI), the SEFD meets or exceeds science requirements over approximately 16% of the observing band, and is within 10% of the science requirements over an additional 17% of the band (such that the SEFD exeeeds, meets, or is within 10% of the science requirements over a total of 33% of the observing band). Simulations suggest that UWBR will provide a net improvement for high-precision pulsar timing projects like NANOGrav, and a substantial improvement for projects that are currently using single, narrow-band receivers to observe pulsars and FRBs. UWBR also opens a new 3–4 GHz frequency window for the GBT, providing access to molecular emission from the CH radical, and the wide bandwidth covers a large number of radio recombination lines (RRLs) that can be used to study star forming regions and the interstellar medium (ISM). Given all of these benefits, UWBR is being released for general scientific use.

In this report we provide a brief technical overview of UWBR and then present the results of scientific commissioning observations. These included SEFD, $T_{\rm sys}$ and gain measurements; demonstrative observations of pulsars, extragalactic HI emission, RRLs, and CH; and characterization of UWBR's beam, calibration noise diode values, and polarization properties. We also derive a new focus tracking model for prime focus receivers, verify the predicted phase center, and charcterize the spillover contribution and $1/f$ noise of the receiver.

Contents

Changelog

1.0 Lynch et al. (2026-06-26) — Initial published version.

Figure 1: The UWBR feed in various states of assembly. Clockwise from upper left: The lower feedhorn with the ridges and dielectric spear; the assembled feedhorn and corrugations (the spear is not installed); the lower feedhorn with the vacuum window installed; the fully assembled receiver during testing in the Outdoor Test Facility.

1 Overview of UWBR

1.1 Hardware and IF System

UWBR utilizes a quad-ridge feed design. The feedhorn is smooth (unlike many other GBT receivers that have a corrugated feedhorn), with four ridges along the interior. A quartz dielectric spear is situated along the center axis of the feed. A quartz-fabric vacuum window sits inside the throat of the feed, at the termination of the ridges and spear. This point in the receiver also marks the thermal gap between the components at cryogenic and ambient temperature. Finally, a corrugated cone sits at the end of the feedhorn, forming the aperture of the receiver. These components of the feedhorn act together to provide acceptable performance over the full observing band: at low frequencies the aperture mitigates over-illumination of the GBT primary reflector and subsequent pickup of ground radiation, at intermediate frequencies the quad-ridge design provides broadband sensitivity, and at the highest frequencies the dielectric spear prevents under-illumination of the GBT primary reflector and subsequent loss of gain. Pictures of the feed are show in Fig. 1.

UWBR samples orthogonal linear polarizations. It does not contain a hybrid and cannot natively produce dual circular polarizations. Stokes V can be measured from the cross-product of the two linear polarization channels.

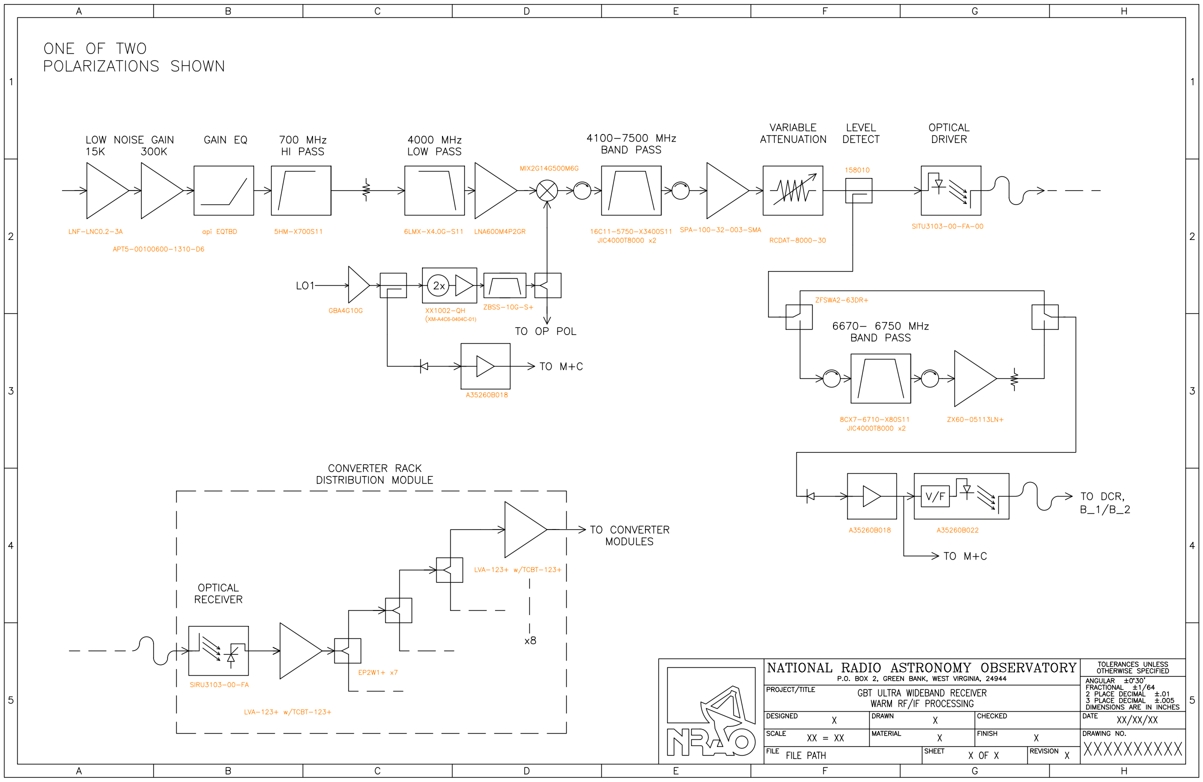

Figure 2: The UWBR IF system, shown up to the DCR and CR.

UWBR uses a commercial differential low noise amplifier (LNA) produced by Low Noise Factory. The LNA and other cryogenic components are cooled by two refrigerators. The frontend box includes a 20-in extension drum that ensures the phase center of the receiver can be aligned with the GBT's prime focal point over nearly all elevations and frequencies. The frontend box also houses an ODROID board which acts as an analog to digital (AD) and digital to analog monitor and control system for the receiver.

UWBR is installed at the GBT's prime focus via the Sterling mount. This mount can provide three axes of motion: axial (along the axis of the GBT's primary reflector, also known as Y), lateral (in elevation, also known as X), and paralactic (rotation about the axial direction). However, in practice the paralactic axis is not used, and in fact *cannot* be used without damaging power, cryogenic, and networking cables connected to the receiver. As a safety precaution, when UWBR is installed paralactic motion of the Sterling mount is disabled.

Calibration signals are injected into each polarization channel via a broadband noise diode. The calibration diode has both a low and high power state and can be controlled via the GBT's standard switching signal distribution system.

The radio frequency (RF) signal from UWBR is up-converted to an intermediate frequency (IF) by mixing a signal from the GBT's local oscillator (LO). A multiplier doubles the LO frequency before mixing with the UWBR RF signal. UWBR has a direct RF over fiber connection to the Digital Continuum Receiver (DCR). This signal path includes a selectable 80 MHz-wide filter that is used by default for pointing and focusing scans. When not using this direct connection to the DCR, UWBR has a direct connection to the GBT converter rack (CR). This signal path includes a 4.1-7.5 GHz IF filter. Unlike most other GBT receivers, UWBR does *not* make use of the IF Rack. Once signals from UWBR reach the CR they can be routed to VEGAS and other GBT backends in the same way as other GBT receivers. A block diagram of the IF system is shown in Fig. 2.

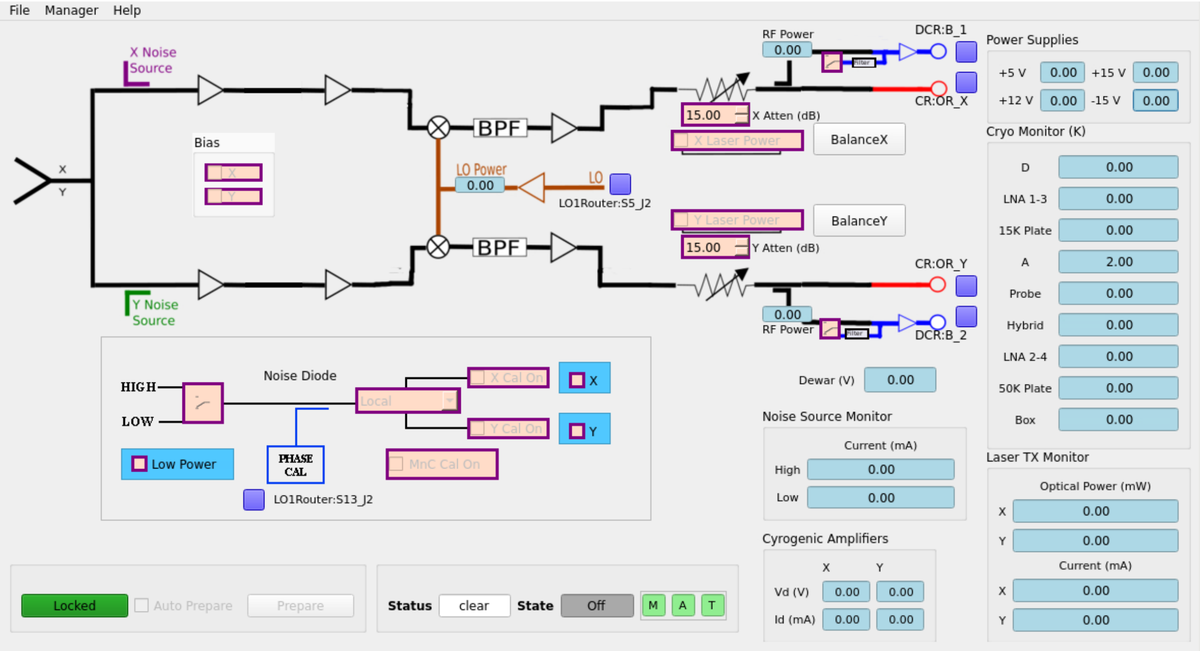

RF Power 0.00

15.00 X Atten (dB)

LO Power 0.00

15.00 Y Atten (dB)

RF Power 0.00

Dewar (V) 0.00

Power Supplies

+5 V 0.00 +15 V 0.00

+12 V 0.00 -15 V 0.00

Cryo Monitor (K)

D	0.00
LNA 1-3	0.00
15K Plate	0.00
A	2.00
Probe	0.00
Hybrid	0.00
LNA 2-4	0.00
50K Plate	0.00
Box	0.00

Noise Source Monitor

	Current (mA)
High	0.00
Low	0.00

Laser TX Monitor

	Optical Power (mW)
X	0.00
Y	0.00

	Current (mA)
X	0.00
Y	0.00

Cyrogenic Amplifiers

	X	Y
Vd (V)	0.00	0.00
Id (mA)	0.00	0.00

Status clear **State** Off

Figure 3: The UWBR pyCLEO application. Note that the receiver Manager was in an off state when this image was captured.

1.2 Monitor and Control Software

UWBR has a dedicated GBT software Manager that monitors and controls temperature and power sensors, amplifiers and attenuators, filters, and the noise diodes. This manager follows the same conventions as other GBT Managers. The Manager runs on a GBO computer named `fire`. The Manager itself is controlled via Task Master in the same way as other GBT Managers.

A pyCLEO application provides a graphical interface to the UWBR Manager. It's behavior is similar to that of other CLEO applications. A screenshot of the UWBR pyCLEO application is shown in Fig. 3. Sampler values are logged via `sampler2log` and can be displayed using the `gbtlogview` application.

2 Commissioning Observations

We performed final UWBR commissioning observations over 19 observing sessions from 19 November to 10 December, 2025. Detailed observing logs, data analysis scripts, reduced data, and plots can be found in `/users/rlynch/UWB/Comm`
Commissioning observations consisted of:

- On-sky measurements of the SEFD, $T_{\rm sys}$, and gain.
- Observations of several well-known pulsars.
- Position-switched observations of the CH radical in W51E.
- Position-switched observations of Hα recombination lines in M42.
- Position and frequency-switched observations of extragalactic HI in UGC 5316.
- A 2-D map of UWBR's main beam.

- Observations of a bright pulsar used to derive Mueller/Jones matrix parameters, as well as observations of a pulsar with well known polarization properties that we used as a check of the calibration solution.
- SEFD measurements as a function of axial focus position, which we use to determine the optimal focusing frequency for wide-band observations.
- Axial and lateral focus measurements used to derive focus tracking models.
- Measurements of the axial and lateral phase center of the receiver.
- Astronomical verification of laboratory-measured $T_{\rm cal}$ values.
- Tipping scans used to measure $T_{\rm spill}$.
- Observations of the North Celestial Pole used to measure $1/f$ noise.

Due to time constraints, we did not derive a new pointing model as part of commissioning observations. Based on our commissioning observations the existing prime focus pointing model is adequate for science observations. However, we recommend deriving a new pointing model as an early post-commissioning activity.

In the follow sections we present the results of each of the above commissioning activities.

3 SEFD, $T_{\rm sys}$, and Gain Measurements

The fundamental observable performance metric we use for UWBR is the SEFD, which is defined as $T_{\rm sys}/G$, where $T_{\rm sys}$ is the system temperature and G is the gain. We measured the SEFD by observing several stable, standard flux calibrators, namely 3C196, 3C286, and 3C295. The flux density of each source as a function of frequency, $S_{\rm src}(\nu)$, was taken from the spectral fits of Perley et al. (2017). We observed each calibrator source along with a position offset by 1° in azimuth and calculated the SEFD as

$$\mathrm{SEFD} = S_{\rm src}\left(\frac{\mathrm{OFF}}{\mathrm{ON}-\mathrm{OFF}}\right) \tag{1}$$

where OFF and ON are the uncalibrated counts at the offset position and the position of the source, respectively[1]. We performed these observations using the VEGAS backend in spectral line Mode 1 and using the coherent dedispersion pulsar mode `c1500x1024uwb`. In each case we sampled three separate spectral windows, each with 1024 frequency channels. Because VEGAS has a usable bandwidth of 1250 MHz, the low and high frequency windows overlapped the middle window by 187.5 MHz, and we discarded the overlapping regions during processing along with the lower and upper edges of the first and third window, resulting in a final sampled bandwidth of 3375 MHz.

To determine the $T_{\rm sys}$ and G we used the receiver noise diodes as a calibration source. Diode temperatures as a function of frequency, $T_{\rm cal}(\nu)$, were taken from laboratory measurements provided by GBO engineers (but see §3.2 for astronomical confirmation of these laboratory-measured values). The frequencies at which $T_{\rm cal}$ were measured are not necessarily the same as those of our astronomical observations, so we used a simple linear interpolation to obtain $T_{\rm cal}$ at the observed frequencies. We then calculated the system temperature as

$$T_{\rm sys} = T_{\rm cal}\left(\frac{\mathrm{CALOFF}}{\mathrm{CALON}-\mathrm{CALOFF}}\right) \tag{2}$$

where CALOFF and CALON are the uncalibrated counts with the noise diode off and on. We took care to only use the off-source scans when determining $T_{\rm sys}$ to avoid contribution from the calibrator source. We measured $T_{\rm sys}$ independently using both the low and high power state of the noise diodes. Finally, the gain was calculated as

$$G = \frac{T_{\rm sys}}{\mathrm{SEFD}} \tag{3}$$

---

[1] Note that we use the usual GBT convention and define the total SEFD, $T_{\rm sys}$, and G as the *average* of the two polarization channels. This differs from some conventions appearing in the literature which define these parameters in terms of the *sum* of the two polarization channels.

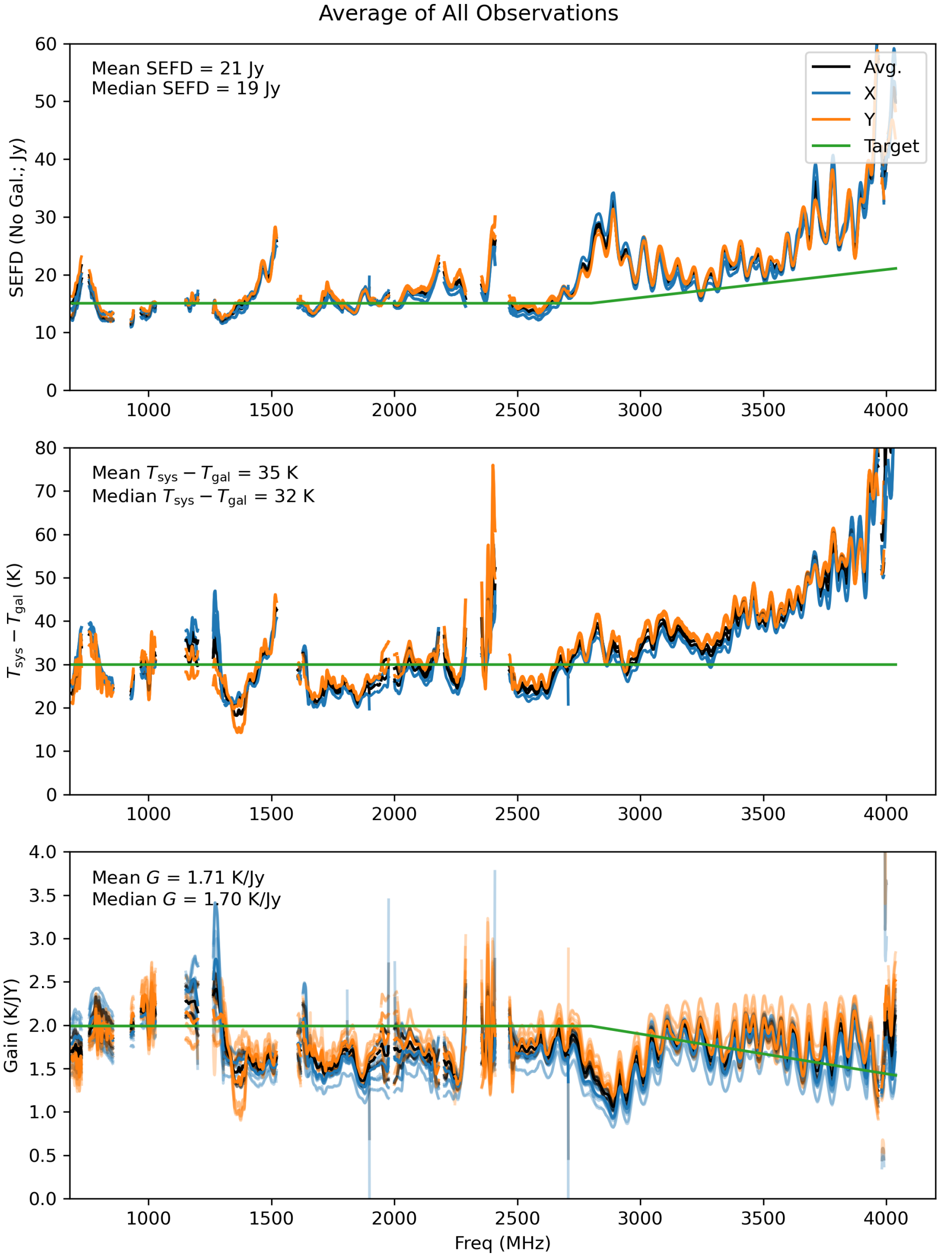

Figure 4: The SEFD, $T_{\rm sys}$, and gain of UWBR in its final configuration. Here we show the average of observations using 3C196, 3C286, and 3C295 as calibration sources, using both the low and high power state of the noise diodes and two different VEGAS modes. Galactic background has been subtracted. Both the X and Y polarization are shown independently along with the average of both polarizations. The targets for each quantity are also shown. Data from each individual source and noise diode state are plotted as semi-transparent lines, while the average over all sources and diode states are shown as opaque lines. Regions most heavily impacted by RFI have been excised.

Figure 4 shows the final results averaged over all three calibrator sources, both VEGAS modes, and both noise diode states. We show results for both polarizations independently, as well as the average of the two polarizations. Gaps in the data are a result of manually excising channels contaminated by RFI. For reference, target parameters are plotted as well ($\mathrm{SEFD} = 15$–20 Jy, $T_{\rm sys} = 30$ K (with no Galactic background contribution), and $G = 2$–1.43 K/Jy). Note that for the purposes of these calculations we have subtracted the Galactic background contribution at the position of each calibrator source. The Galactic background was taken from Haslam et al. (1982)[2].

UWBR currently performs better than the target SEFD over 16% of the observing band and is within 10% of of the target SEFD over an additional 17% of the band (such that the SEFD exeeeds, meets, or is within 10% of the science requirements over a total of 33% of the observing band). While this is the best performance we have achieved with UWBR thus far, it currently does not meet the target specifications, which were defined such that UWBR would provide a substantial improvement in high-precision pulsar timing. Before recommending UWBR for scientific use, it is important that we build confidence in its ability to provide a net overall pulsar timing benefit relative to other GBT instruments.

3.1 Pulsar Timing Simulations

UWBR's primary scientific motivation is improving sensitivity to nanohertz-frequency gravitational waves via high-precision pulsar timing. This is the focus of the North American Nanohertz Observatory for Gravitational Waves (NANOGrav)[3], which will also be one of the primary users of UWBR.

There are a number of effects that must be incorporated into pulsar timing models to achieve a long-term pulsar timing RMS that is low enough to detect the subtle effects of gravitational waves. The most relevant for this analysis are changes in the column density of free electrons along the line of sight to a pulsar, also known as the dispersion measure (DM). These free electrons lead to a frequency-dependent dispersive delay of the pulsar's signal given by

$$\Delta t_{\rm DM} = k_{\rm DM}{\rm DM}\left(\frac{1}{f_1^2} - \frac{1}{f_2^2}\right) \tag{4}$$

where $k_{\rm DM}$ is a constant. The precision needed by NANOGrav requires measuring DM over a wide bandwidth. When UWBR development began NANOGrav used the PF800 and L-Band receivers for all pulsars observed with the GBT to achieve the necessary wide-band coverage, with observations separated by up to a few days. UWBR was expected to improve observing efficiency, effectively doubling the observing time per pulsar, and to reduce systemic errors by providing an instantaneous DM measurement over a wider bandwidth. The wide bandwidth was also expected to reduce radiometer noise.

NANOGrav's observing strategy changed following the collapse of the Arecibo Telescope and the completion of the Canadian HI Intensity Mapping Experiment (CHIME) — more pulsars are now observed using the GBT, and all of these are observed using the L-Band receiver. Low frequency data for the majority of pulsars is now provided via daily CHIME observations, with the GBT's PF800 receiver used for a smaller number of low-declination sources. A few sources are also observed with the VLA at S-Band.

We compared the predicted pulsar timing RMS for NANOGrav's existing timing program to a program in which UWBR replaces GBT L-Band and, where applicable, PF800 observations. We assumed that CHIME and VLA data would continue to be used in the same way. We used the formalism of M. T. Lam et al. (2018) to predict the long-term timing RMS using the measured, on-sky SEFD for UWBR, L-Band, PF800, and CHIME, and using pulsar parameters from the NANOGrav 20 year data release (Cohen, 2025). This framework has been vetted and used by NANOGrav to optimize their observing program following the collapse of Arecibo and in planning for use of the DSA[4]. We used 30-minute scan lengths at L-Band and PF800, and assumed 30-minute scan lengths using UWBR for pulsars currently being observed only with L-Band, and one hour scan lengths with UWBR for pulsars currently being observed with both L-Band and PF800.

Figure 5 shows the RMS ratio for NANOGrav's current program compared to using UWBR. Since we wish to minimize RMS, a ratio greater than one indicates an improvement when using UWBR. The errorbars are not uncertainties, but rather capture the range of possible RMS improvement depending on the magnitude of DM misestimation errors using the current PF800+L-Band strategy (M. Lam, 2025). The upper range of these bars is optimistic (in the sense that the current DM misestimation errors are large and would be reduced using UWBR), and should be treated as an upper limit to the expected improvement. The data points represent the improvement for the median DM misestimation error.

---

[2] We used the `pygdsm` package (Price, 2016) to obtain $T_{\rm gal}$ at the position of each source.

[3] UWBR was funded in part by a grant from the Gordon and Betty Moore foundation awarded to NANOGrav.

[4] https://www.aoc.nrao.edu/~tcohen/research/popsynth.shtml

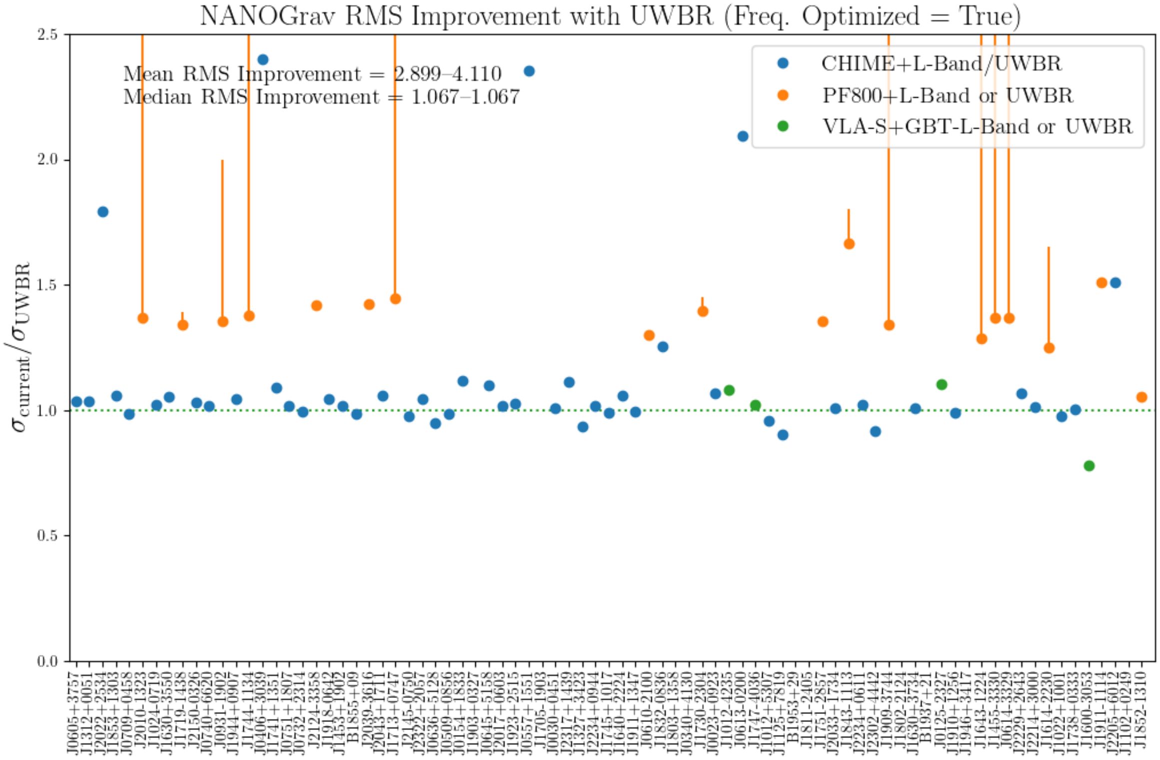

Figure 5: Predicted timing RMS improvement for NANOGrav pulsars when using UWBR vs the current NANOGrav timing program. Error bars represent the possible range of improvement depending on different assumptions for the DM misestimation error when using PF800 and L-Band. See text for details.

The mean RMS improvement is 2.9–4.1× (depending on whether one compares to the median or maximum DM misestimation error) while the median improvement is 1.1×. As expected, pulsars currently observed with both PF800 and L-Band benefit the most from using UWBR, largely because the observing time can be doubled (though in some cases the DM misestimation error can be quite large, and so reducing it offers a substantial potential improvement). Most pulsars currently observed with only L-Band on the GBT benefit from moving to UWBR, though the RMS improvement is modest since CHIME already provides daily low-frequency coverage. Overall, these simulations suggest that UWBR will be a net benefit for NANOGrav.

We stress that most pulsar programs on the GBT do not incorporate CHIME data, or even multi-band observations using PF800. For these projects we expect UWBR to be a *substantial* improvement over using a single receiver. For example, timing RMS using only UWBR is 5.1× lower than when using only L-Band for pulsars in the 20-year NANOGrav data release. Given all of the above, we are confident that UWBR will significantly improve pulsar science on the GBT.

3.2 Astronomical T_{cal} Verification

The T_{sys} presented in §3 was derived using laboratory-measured T_{cal} values, which were in turn measured using a room temperature hot load and liquid nitrogen (LN2) cold load. However, the large aperture of UWBR makes it difficult to obtain a cold load measurement because the pool of LN2 must be large and boils off quickly. We therefore attempted to validate the T_{cal} measurement with an independent astronomical measurement. The goal of these observations was not to supersede the laboratory T_{cal} values but to check them for consistency.

Because the gain of UWBR varies widely across the band and is not known a priori, we chose to derive T_{cal}

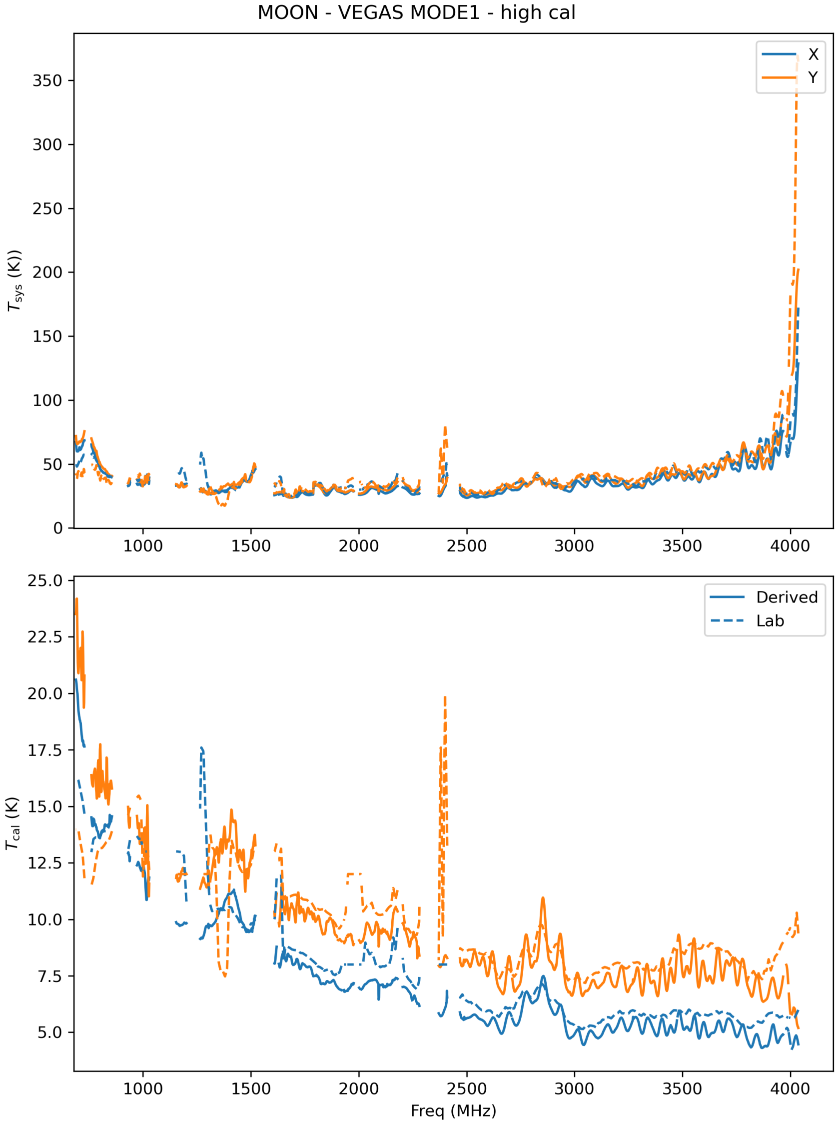

Figure 6: Comparison of laboratory measured $T_{\rm cal}$ values and those derived from observations of the Moon for the high-power noise diode.

values using the Moon as a source with a known physical temperature. We observed at new Moon using VEGAS in spectral line Mode 1, obtaining data with both the high and low powered noise diodes. We used a two-step process, where we first measured $T_{\rm sys}$ as

$$T_{\rm sys} = \frac{\rm OFF}{\rm ON - OFF} T_{\rm moon} \tag{5}$$

where ON is the on-source position, OFF is a reference position (both ON and OFF were with the noise diodes in an off state), and $T_{\rm moon}$ is the temperature of the moon and was calculated as

$$T_{\rm moon} = T_{\rm moon,ref} \left(\frac{\nu}{1.4\ \rm GHz}\right)^{\alpha} \tag{6}$$

where $T_{\rm moon,ref} = 233$ K and $\alpha = -0.1$ (Zhang et al., 2012). These authors report a range of $-0.05 \leq \alpha \leq -0.15$ depending on the position on the lunar surface, and temperature variations of about 5 K depending on the lunar quadrant, with a maximum of 257 K observed near the lunar equator. We do not attempt to deal with these

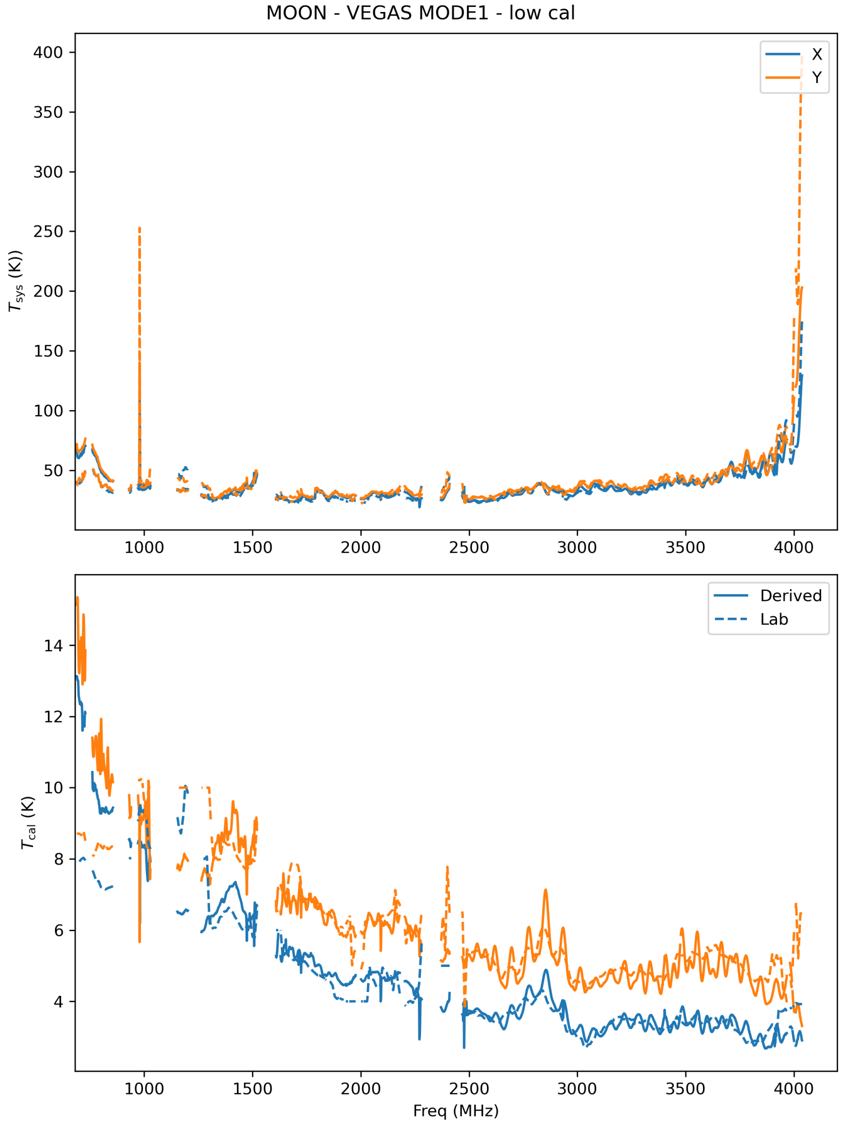

Figure 7: Comparison of laboratory measured T_{cal} values and those derived from observations of the Moon for the lower-power noise diode.

complications here, since our goal is only to provide an approximate check of the laboratory derived T_{cal} values. Having determined T_{sys} using the Moon, we derive T_{cal} as

$$T_{\mathrm{cal}} = \frac{\mathrm{CALON} - \mathrm{CALOFF}}{\mathrm{CALOFF}} T_{\mathrm{sys}} \tag{7}$$

where CALON and CALOFF refer to the state of the noise diodes (in both cases we used the off-source position).

Results are shown in Figs. 6 and 7 for the high and low noise diodes, respectively. Overall we find very good agreement between astronomically derived and laboratory measured T_{cal} values, with some deviation in the low-power noise diode at frequencies $\lesssim 1$ GHz. We conclude that the laboratory measured T_{cal} values are accurate and suitable for calibration, though calibration errors may be higher at low frequencies.

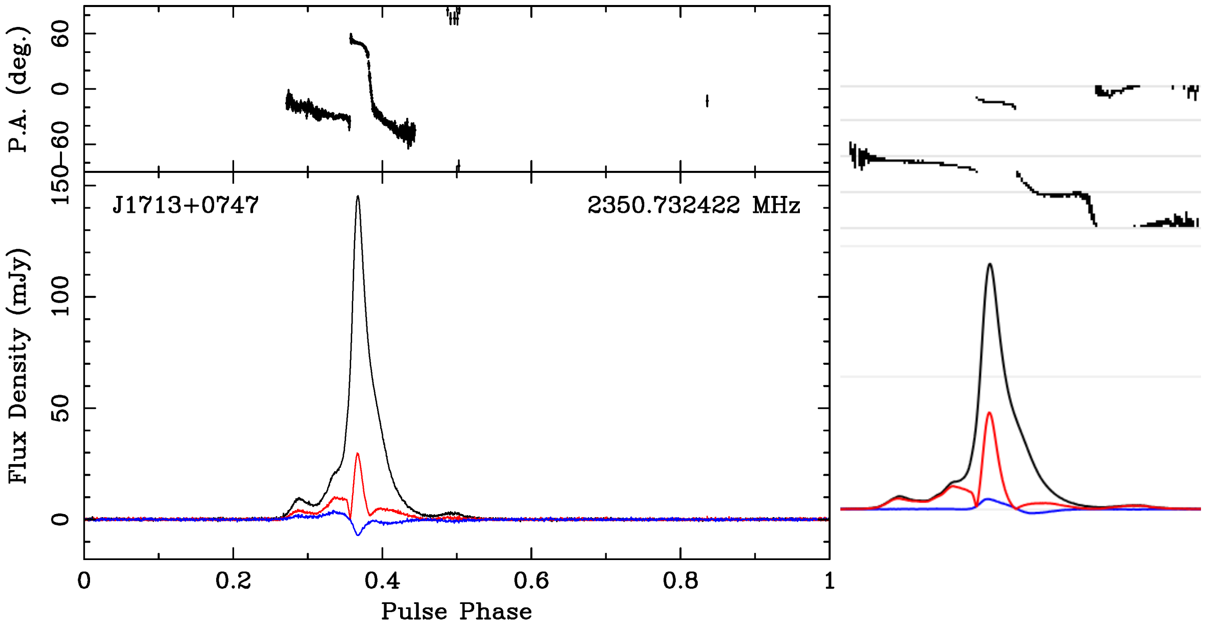

Figure 8: *Right:* UWBR integrated profile of PSR J1713+0747. The data have been full flux and polarization calibrated, corrected for Faraday rotation, and RFI has been excised using PSRCHIVE tools. Linearly polarized flux is plotted in red and circularly polarized flux is plotted in blue. *Left:* A comparison L-Band pulse profile of J1713+0747 obtained with Murriyang, CSIRO's Parkes radio telescope (data from Dai et al. (2015); image retrieved from the European Pulsar Network Database of Pulsar Profiles). The phase range has been restricted for clarity. Note that the sign of circular polarization is different; we follow the `PSRCHIVE` convention (see §9.1). Other small differences are likely due to profile evolution over the different frequency ranges of the two datasets.

4 Pulsar Observations

We observed three well-known millisecond pulsars (MSPs): PSRs J1713+0747, B1937+21, and J1903+0327. Each observation was approximately 30 minutes in duration. Data were calibrated using 3C295 and the `pcm` polarization model described in §9. For each pulsar we corrected for Faraday rotation using the rotation measure listed in the Australia National Telescope Facility Catalogue Database[5] (Manchester et al., 2005). We also used the PSRCHIVE command `paz` to automatically remove RFI using the median smoothed difference method. Figure 8 shows a representative pulse profile for PSR J1713+0747. In Fig. 9 we show the total intensity as a function of frequency and pulse phase, along with the frequency ranges covered by other GBT receivers typically used for studying pulsars. In Table 1 we report 1400 MHz flux densities of each pulsar as recovered with UWBR to those in the NANOGrav 12.5 year data release (Alam et al., 2021). We used the PSRCHIVE command `pdv` to extract the 1400-MHz flux density after reducing the frequency resolution to 16 channels (each covering approximately 200 MHz). Because PSR J1903+0327 also has a broad profile and lower flux density, we also reduced the pulsar phase resolution to improve S/N. We report the median NANOGrav flux as well as the range encompassing the 16th and 84th percentiles. Pulsar flux density fluctuates from epoch to epoch due to interstellar scintillation, so we do not expect exact agreement between our single-epoch measurements and published values. Nevertheless, in

---

[5] https://www.atnf.csiro.au/research/pulsar/psrcat/

Table 1: 1400 MHz Flux Densities

PSR	UWBR (mJy)	NANOGrav (mJy)
J1713+0747	7.178 ± 0.009	$4.3^{+4.1}_{-2.3}$
B1937+21	12.04 ± 0.01	$12.4^{+4.1}_{-3.3}$
J1903+0327	0.545 ± 0.008	$0.69^{+0.10}_{-0.06}$

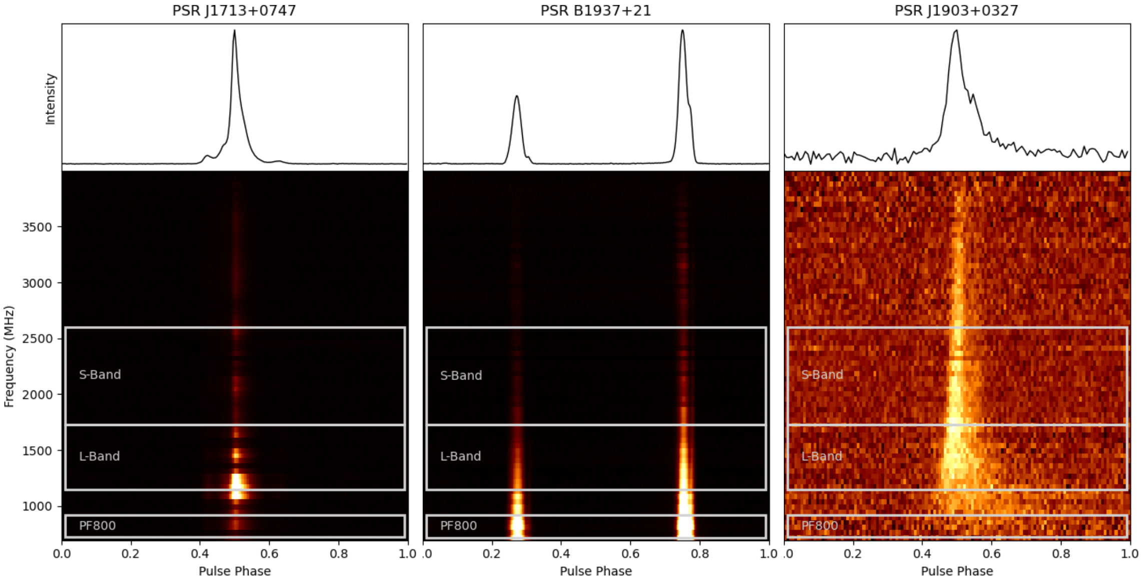

Figure 9: Total intensity as a function of pulse phase and frequency for PSRs J1713+0747, B1937+21, and J1903+0327. The data have been fully flux calibrated and RFI has been removed, but we have adjusted the scaling to improve visibility of the pulsars at high frequencies. The drop in flux at high frequencies for J1713+0747 and B1937+21 is intrinsic to both pulsars. J1903+0327 has a flatter spectral index and so is not as faint at high frequencies relative to low frequencies. The pulse broadening of J1903+0327 is a result of interstellar scattering.

each case the flux we measure is within the range reported by (Alam et al., 2021).

5 Observation of CH in W51E

UWBR opens a new 3–4 GHz frequency window for the GBT, and with it access to emission from the CH radical. To demonstrate this new capability we observed W51E using VEGAS in Modes 6, 9, and 10 using position switching. We spent 12 minutes at both the on and off source position in each mode, using a 1° offset in azimuth for the off-source position. CH emission is expected at three rest frequencies: 3.264, 3.335, and 3.349 GHz, with a source velocity of ∼60 km/s (Jacob et al., 2024). Figure 5 shows the detection of these three lines using UWBR in Mode 10 (note the continuum background emission is also visible as a non-zero baseline). The data were averaged over time and polarization and smoothed by 6 channels. In Fig. 11 we show a detection of the same lines from Jacob et al. (2024). The line shapes and velocities obtained with UWBR are in good qualitative agreement with published values.

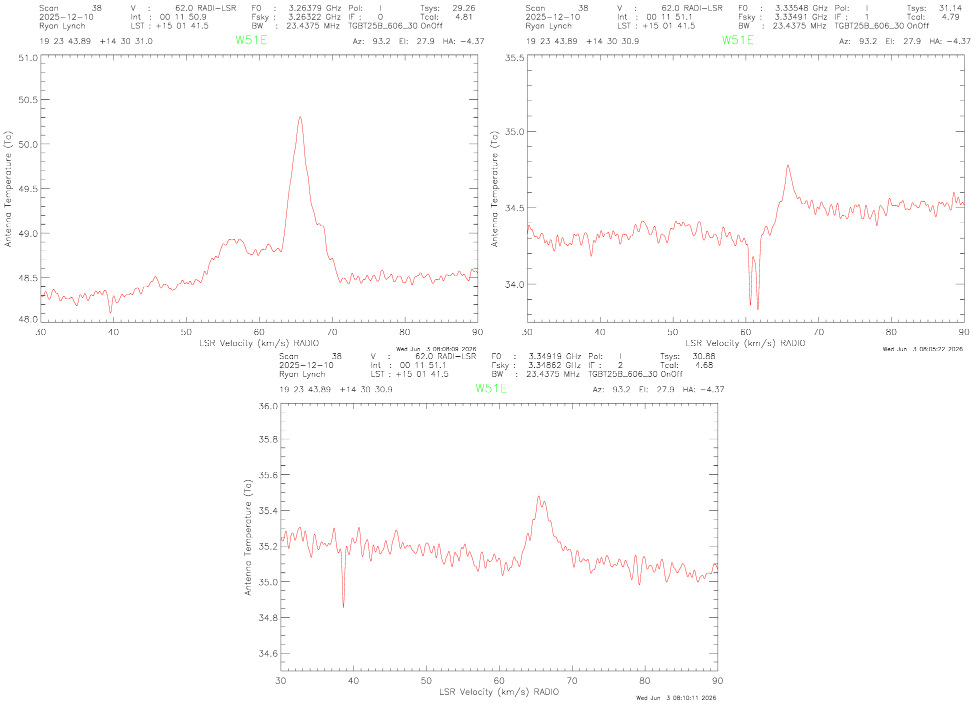

Figure 10: Detections of CH in W51E using UWBR. The source velocity is ~ 60 km/s.

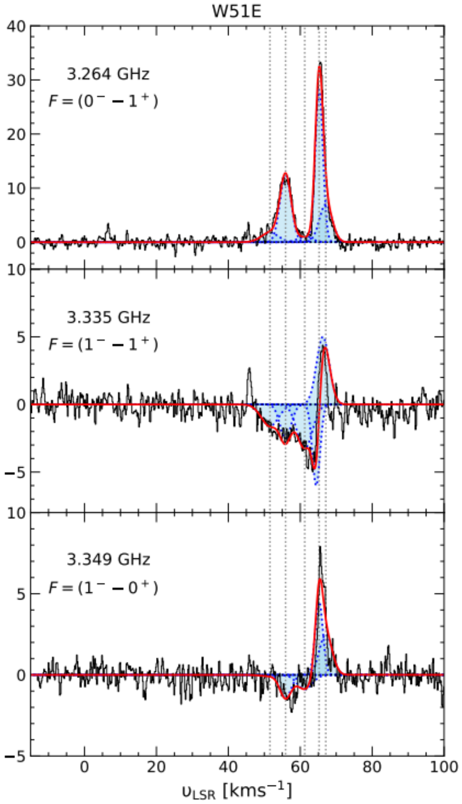

Figure 11: CH detected in W51E using uGMRT (see Jacob et al., 2024). The y-axes are T_a in units of K.

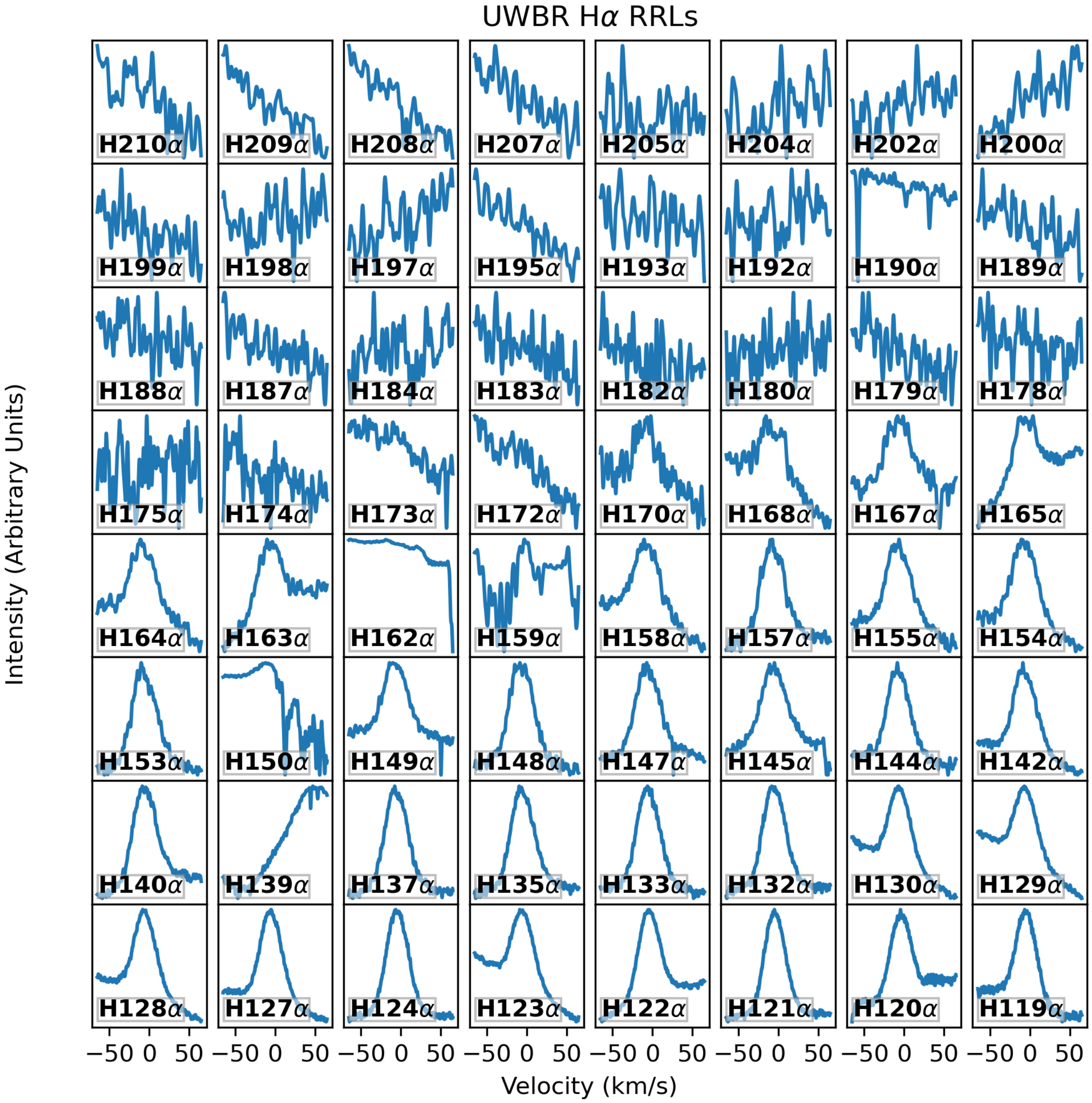

Figure 12: Hα RRLs observed in M42 with UWBR. See text for details.

6 Hα Recombination Line Observations of M42

UWBR's wide bandwidth covers 94 Hα recombination lines, making it an excellent instrument for studying the star forming regions from which this emission arises. To demonstrate this capability we observed 64 Hα RRLs (the maximum that can be simultaneously observed with VEGAS) in M42. We used VEGAS Mode 24 with position switching, and observed the on- and off-source positions for 750 seconds each. Fig. 12 shows all 64 lines. Lines at frequencies above 1.327 GHz (corresponding to H170α) are clearly detected with the exception of H162α, H159α, H150α, and H139α — further investigation showed that these lines are impacted by strong RFI. Lines below 1.281 GHz (corresponding to H172α) are not clearly detected. This is likely due to the fact that line intensities below this frequency drop as the nebula becomes optically thick. It is also possible that the 1° position offset that we used was not large enough to completely avoid some on-source contribution at lower frequencies.

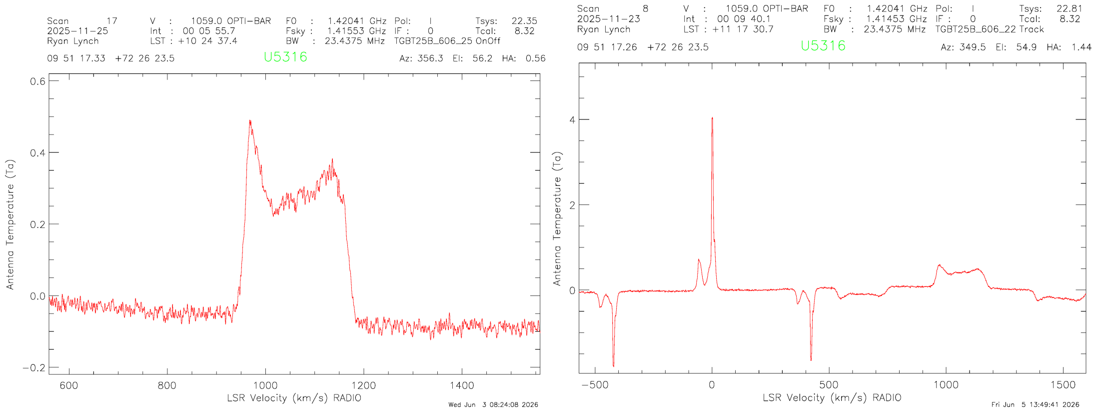

Figure 13: HI detected in UGC 5316 with UWBR using position switching (left) and frequency switching (right). Galactic HI is also visible in the frequency-switched spectrum. See text for details.

We verified that the IF setup was correct and that we obtain good $T_{\rm sys}$ with this setup when observing blank sky, so we do not believe that the lack of detections below 1.2 GHz is due to an instrumental error. We conclude that UWBR is ready to be used for RRL observations.

7 Extragalactic HI Observations

The GBT's L-Band receiver is more sensitive than UWBR over narrow bandwidths, and we expect L-Band to continue to be the primary receiver used to study HI and OH. Nevertheless, observations of HI offer a good point of comparison between UWBR and L-Band. We observed UGC 5316, which is a circumpolar galaxy with a classic double-peaked HI emission profile that is frequently used as a test source at the GBT. We observed using both position and frequency switching using VEGAS in Modes 6, 9, and 10. For the position-switched observations we used an offset of 1° in azimuth, and for the frequency switched observations we used a frequency throw of 1 MHz. Fig. 13 show the resulting position-switched and frequency-switched spectra taken in Mode 10. UGC 5316 is clearly detected in HI emission, with residual emission from Milky Way HI also visible. Spectral baselines are fairly flat when using both frequency and position switching in these modes. In wider bandwidth modes there is more baseline structure. We recommend using narrower-band VEGAS modes for spectroscopic observations when possible.

8 Beam Map

We produced a full 2-D beam map as a function of frequency by using the Astrid `DecLatMap` procedure and the bright point source 3C147. This source is very compact and a good choice for mapping UWBR's beam. An animation showing the evolution of the beam as a function of frequency can be found at `/users/rlynch/UWB/Commissioning/2023_May/UWBR_beam_map_interp.mp4`. In Figure 14 we show maps at select frequencies.

Overall, UWBR's beam is well behaved, though significant side lobes are visible around approximately 2.7–3 GHz, especially in the X polarization. These side lobes are the result of transverse modes excited in the throat of the receiver, which are also responsible for the drop in gain over the same frequency range (see Fig. 4). There is also some asymmetry in the beam at frequencies $\lesssim$ 1.7 GHz, though the beam is more symmetrical when averaging the two polarizations.

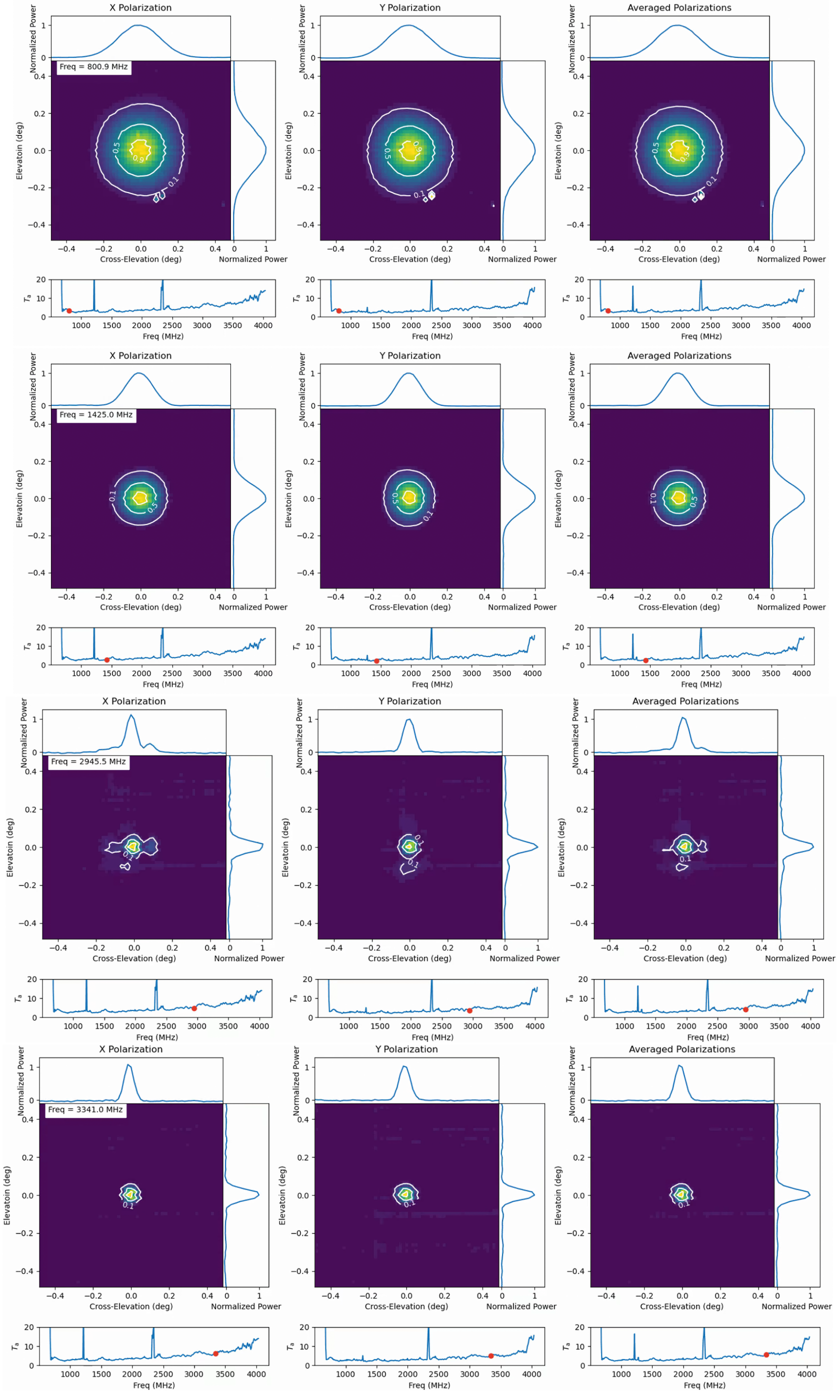

Figure 14: UWBR beam maps using the compact source 3C147 at approximately 800, 1425, 2945, and 3341 MHz. We chose these frequencies to highlight the shape of the UWBR beam at the lower end of its range, near the HI line, in a range where there are non-Gaussian side lobes, and near the CH line, respectively.

9 Detailed Polarization Calibration

We observed the bright pulsar B1929+10 over a range of paralactic angles to derive a full polarization calibration solution. We used VEGAS with coherent dedispersion in Mode c1500x1024uwb, covering the full UWBR band.

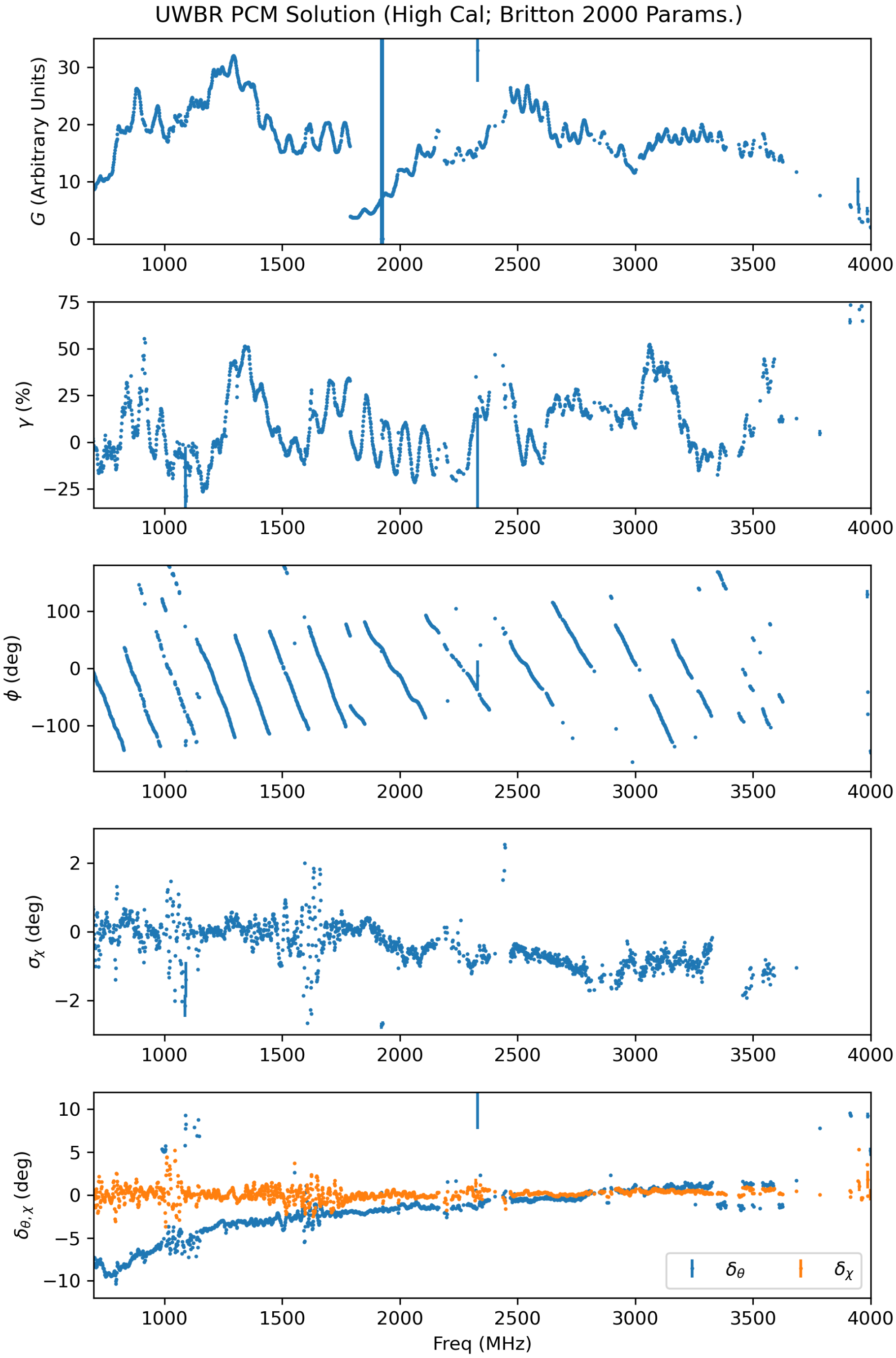

Figure 15: Polarization calibration solution using the high-power noise diode derived using the PSRCHIVE `pcm` function. See text for details.

We covered hour angles from approximately −03:40 – +04:09, but with a gap between −00:15 – +02:40 during which the scheduled observations were interrupted for a target of opportunity project. However, we believe this is sufficient to measure Muller/Jones matrix parameters, and the gap in hour angle coverage of these scans does not prevent scientific use of the receiver. Nevertheless, it would be useful to repeat these observations with more complete hour angle coverage in the future.

We reduced the data using the PSRCHIVE command `pcm` using recommended options for measurement equation

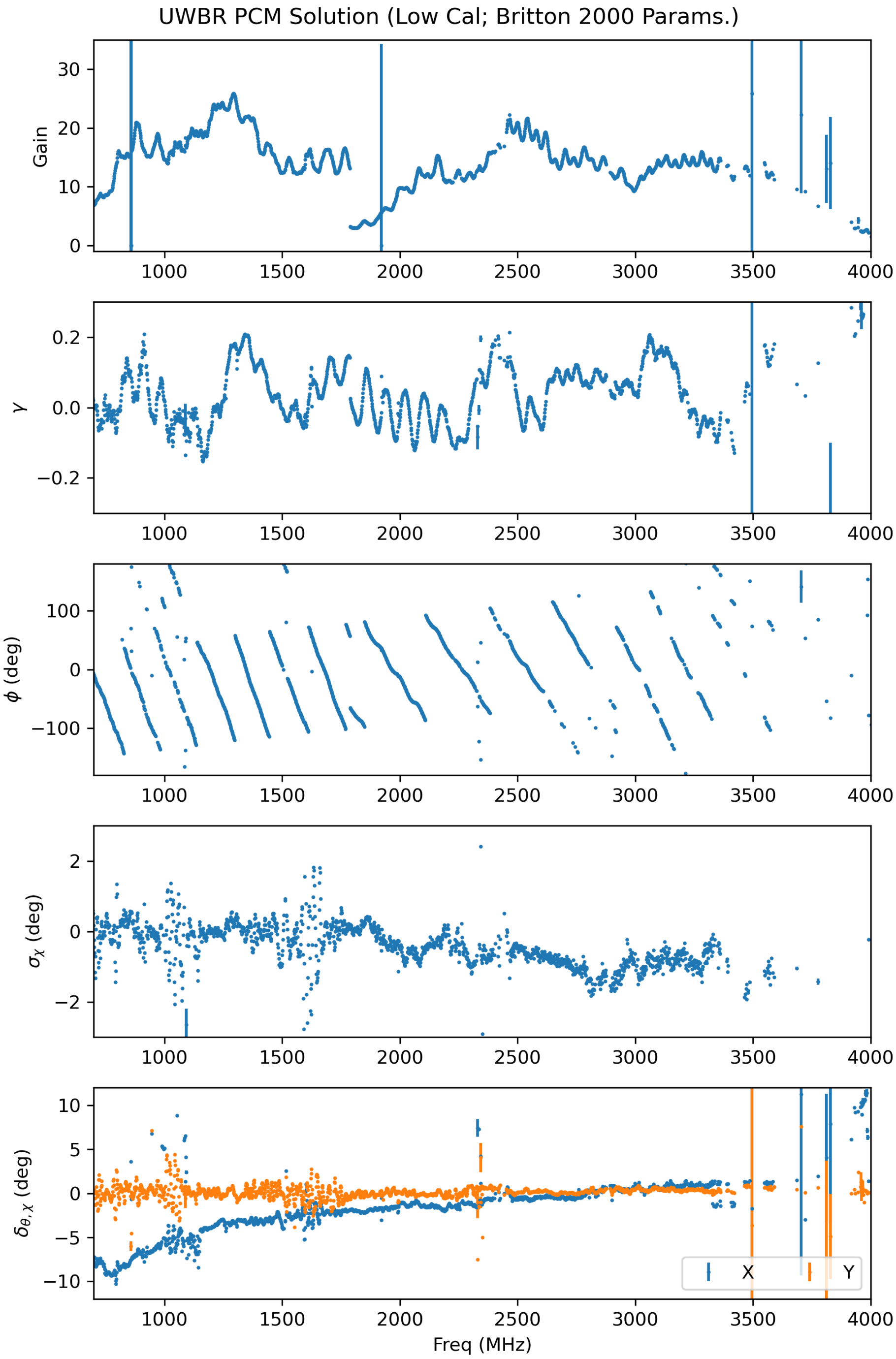

Figure 16: Polarization calibration solution using the low-power noise diode derived using the PSRCHIVE `pcm` function. See text for details.

modeling. Specifically, we used the parameterization defined by Britton (2000) and allowed `pcm` to fit a step-change in noise diode parameters for the two separate scans.

Figs. 15 and 16 show the resulting solutions for the high and low-power noise diode, respectively. Following Britton (2000), the panels show absolute gain, differential gain (γ), differential phase (ϕ), mean ellipticity of the two receptors (σ_χ), and differential receptor orientation angle (δ_θ and differential receptor ellipticity difference (δ_χ). There are a few things to note:

- Error bars derived from the diagonal components of the covariance matrix returned by `pcm` are shown. There are a few points, most noticeable in the absolute gain plot, with large errors, but overall the formal errors are small.
- The slope of ϕ may change at the boundary between different VEGAS ROACH2 boards. This is because the two ADCs can be offset by up to ±3 clock cycles depending on how they are programmed at startup. This is a known behavior in VEGAS, and the offsets remain constant until the ROACH2 is programmed with a new BOF file. The effect can be corrected following standard procedures in which the noise diode is observed before each science source.
- Missing data points are those where the fit failed to converge.

`PSRCHIVE` can also be used to produce Mueller and Jones matrices from these `pcm` solutions.

9.1 Validation of `pcm` Fits

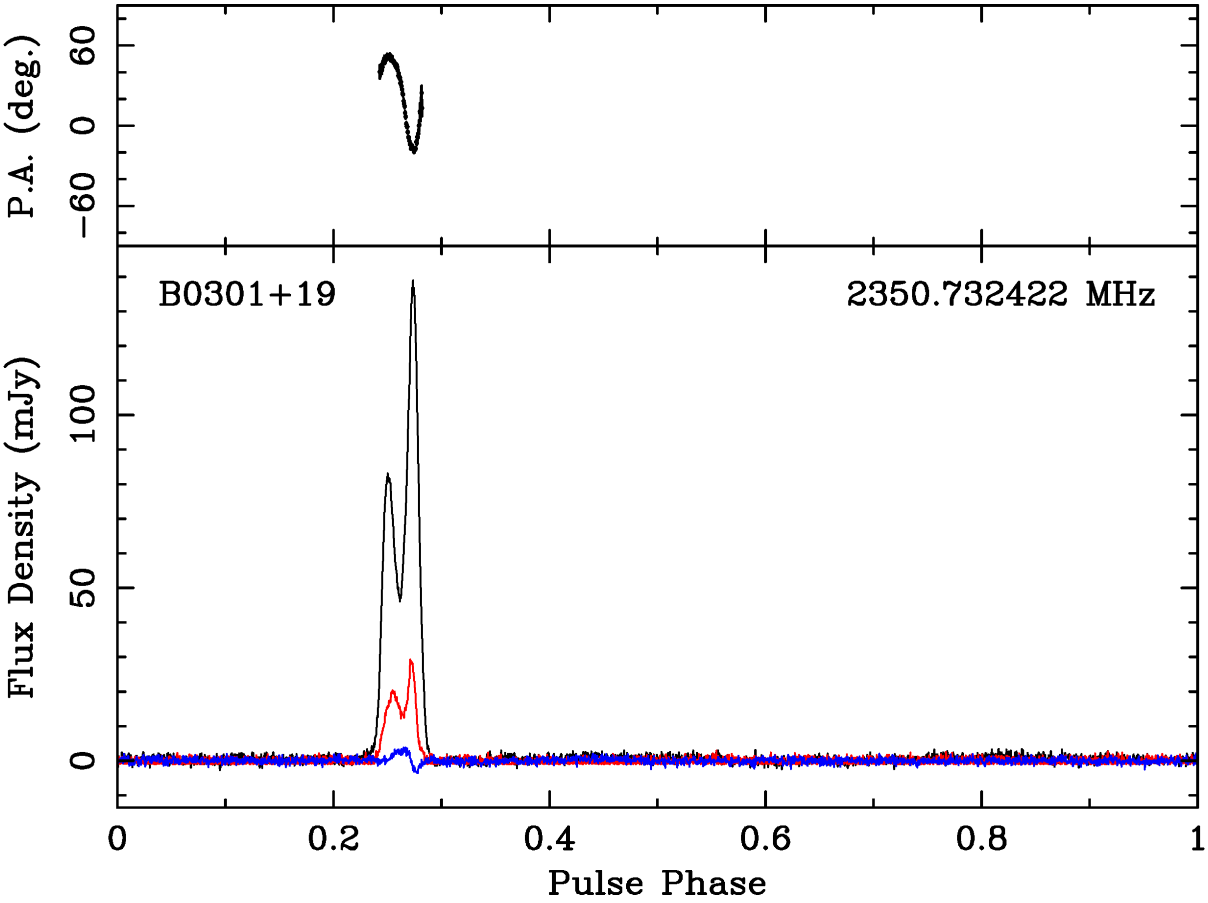

Figure 17: PSR B0301+19 after calibration using the high-power noise diode `pcm` solution. Red curves indicate linearly polarized flux and blue curves indicate circularly polarized flux.

In Fig. 17 we show the pulse profile of PSR B0301+19 after calibration using the above `pcm` solution (in this case we used the high power noise diode). PSR B0301+19 is one of several sources used by van Straten et al. (2010) to check polarization calibration using `PSRCHIVE` tools. In Fig. 18 we show a reference profile from van Straten et al. (2010). The linearly and circularly polarized flux and polarization position angles are in good

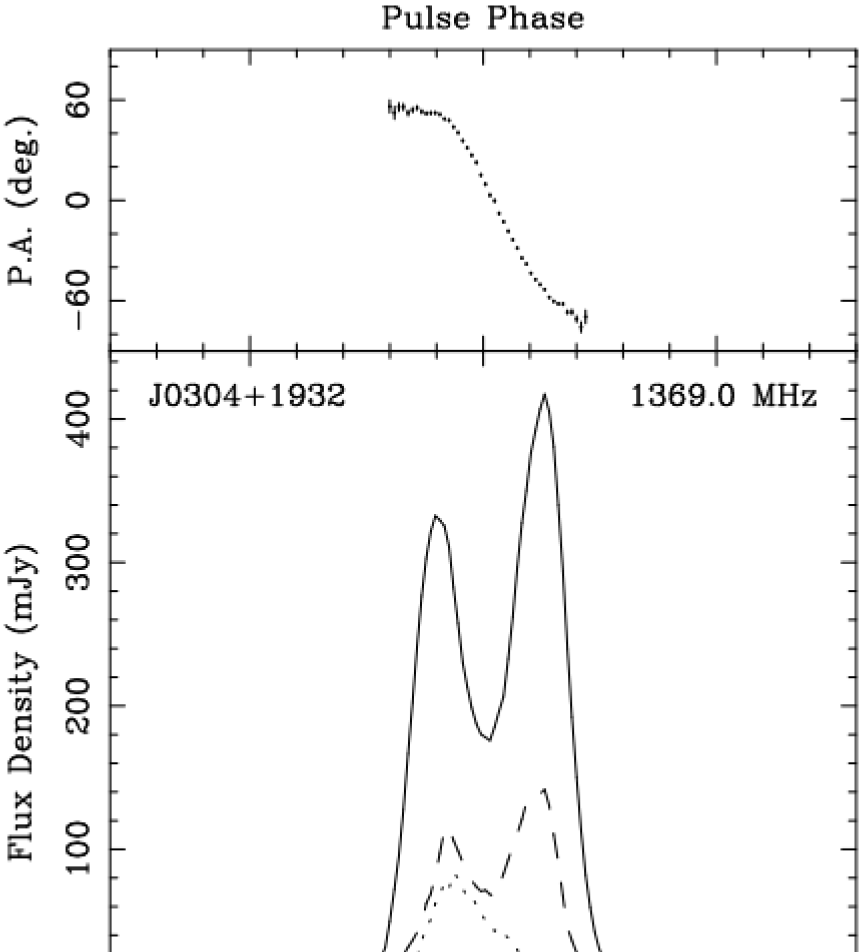

Figure 18: Reference profile of PSR B0301+19 taken from van Straten et al. (2010). The dashed curve is the linearly polarized profile and the dotted curve is the circularly polarized profile.

Table 2: Average SEFD at Various Focusing Frequencies

Freq (MHz)	Mean SEFD (Jy)	Median SEFD (Jy)
740	21	20
980	20	19
1220	20	19
1460	20	19
1700	23	20
1940	22	20
2180	21	19
2420	22	20
2660	20	19
2900	21	19
3140	21	19
3380	21	19
3620	20	19
3860	20	19
3960	20	19

agreement. We atrribute the small differences to profile evolution over the very different frequency coverage of UWBR compared to the 20-cm Parkes data taken from van Straten et al. (2010).

10 Optimal Focusing Frequency

Prior to the development of UWBR the GBT M&C system did not support automatic focus scans and fits for prime focus receivers. However, at the upper range of UWBR's frequency the change in gain as a function of focus offset is significant, and focusing is important to achieve optimal sensitivity. It is therefore important that observers perform a focusing scan when using UWBR.

We determined the optimal focusing frequency for wide-band observations by focusing at different frequencies and then measuring the SEFD using the same approach as outlined in §3. For all scans we observed 3C196 using VEGAS in Mode 1 and the high-power noise diode. Table 2 shows the focusing frequency and average SEFD. The mean and median SEFD do not vary much with focusing frequency, though we note that the gain does vary noticeably at high frequencies depending on the exact focusing frequency. Based on these results we adopted an optimal focusing frequency of 2660 MHz and used this for all wide-band observations presented in this report.

11 Focus Tracking Model

The GBT's prime focus position is elevation dependent (but independent of receiver or frequency) and lies 2204.5 mm from the Sterling mount zero-point when the GBT is at an elevation of 90°. The axial and lateral focus tracking models update the default focus offsets to follow the elevation-dependent focus position. However, because the focus offsets depend on the location of the phase center of the chosen receiver, the focus tracking model can be receiver and frequency dependent. The current prime focus axial and lateral focus tracking models were derived using the PF800 receiver by Balser et al. (2001) and have not been updated since, so we have derived a new axial and lateral focus tracking model using UWBR. We took data for both models as part of the same session, observing 3C196 over a range of elevations from approximately 10° to 80°. Note that focus tracking using the current model was disabled for these observations. We had to interrupt the session while engineers fixed a pinched helium line, leading to a gap in elevation coverage between approximately 30° and 43°. Both the axial and lateral focus tracking models have a functional form of

$$F = a + b\cos E + c\sin E \tag{8}$$

where F is the focus offset, E is the elevation, and a, b, and c are constants.

Table 3: Axial Focus Tracking Model Coefficients

	a (mm)	b (mm)	c (mm)
UWBR X	1062.52 ± 8.32	-251.39 ± 6.39	-42.71 ± 6.56
UWBR Y	1068.73 ± 8.93	-241.42 ± -6.87	-56.62 ± 7.05
UWBR Avg.	1065.63	-246.41	-49.67
PF800 Current	1202.997	-263.703	-84.5007

11.1 Axial Focus Tracking Model

The axial focus tracking model was derived by measuring focus offsets using the `AutoPeakFocus` routine and fitting for the coefficients in Eq. 8. Fig. 19 shows the resulting fits and Table 3 provides the model coefficients. We include the current axial focus tracking model coefficients from Balser et al. (2001) for comparison.

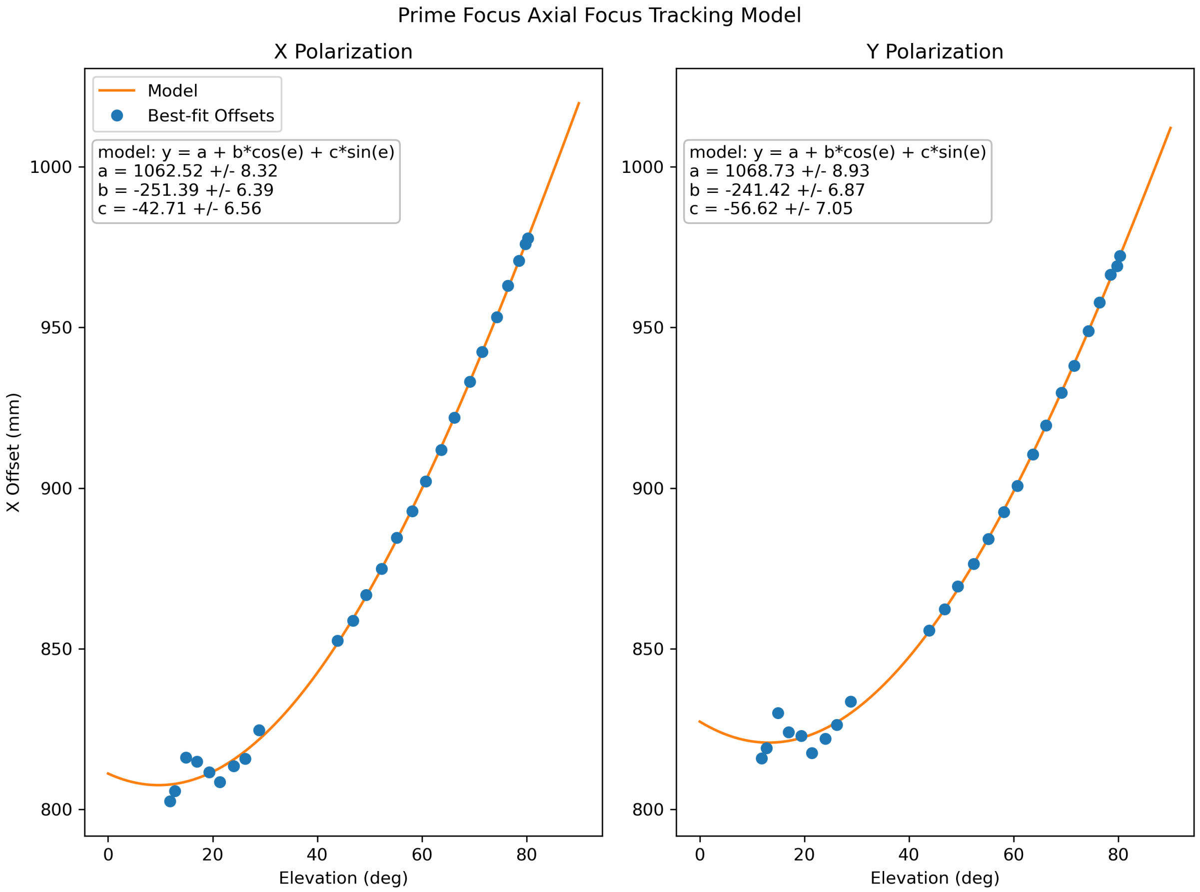

Figure 19: Axial focus offsets as a function of elevation for the UWBR X and Y polarization channels. The best-fit focus tracking model is also shown.

11.2 Lateral Focus Tracking Model

The lateral focus tracking model was derived by manually adjusting the “X” focus axis offsets from 50 to 850 mm in increments of 100 mm. At each offset we performed cross-elevation peak scans using a modified version of the `AutoPeak` routine and recorded the peak $T_{\rm a}$ as determined by GFM pointing fits. We then fit a Gaussian to these

Table 4: Lateral Focus Tracking Model Coefficients

	a (mm)	b (mm)	c (mm)
UWBR X	668.44 ± 19.12	-285.98 ± 14.40	26.49 ± 14.02
UWBR Y	632.09 ± 9.00	-270.27 ± -6.31	5.05 ± 7.06
UWBR Avg.	650.27	-278.13	15.77
PF800 Current	780.797	-329.413	-84.5007

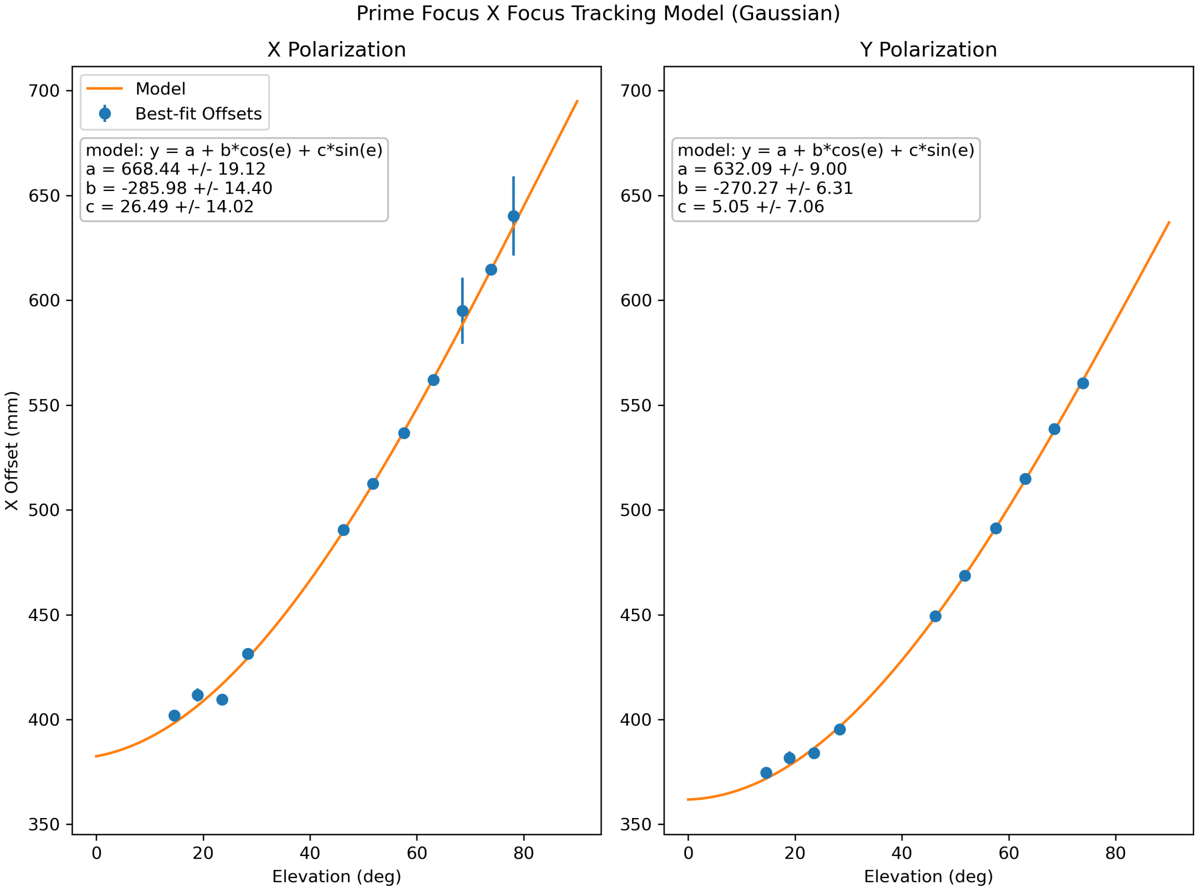

Figure 20: Best-fit lateral focus offsets as a function of elevation for the UWBR X and Y polarization channels. The best-fit focus tracking model is also shown.

T_{a} vs X offset data and took the centroid to be the optimal X offset at that elevation (we used the average elevation over the sequence of cross-elevation peak scans), and used these X offsets when fitting for the coefficients in Eq. 8. Fig. 20 shows the resulting fits and Table 4 provides the model coefficients. We include the current axial focus tracking model coefficients from Balser et al. (2001).

12 Phase Center Measurement

We measured the axial phase center of UWBR as a function of frequency using the same data presented in §10. There are a few subtleties to this process:

1. When focus tracking is enabled, GFM reports focus positions relative to the focus tracking model. To convert the GFM-reported focus offset to the reference frame of the Sterling mount, one must add the GFM

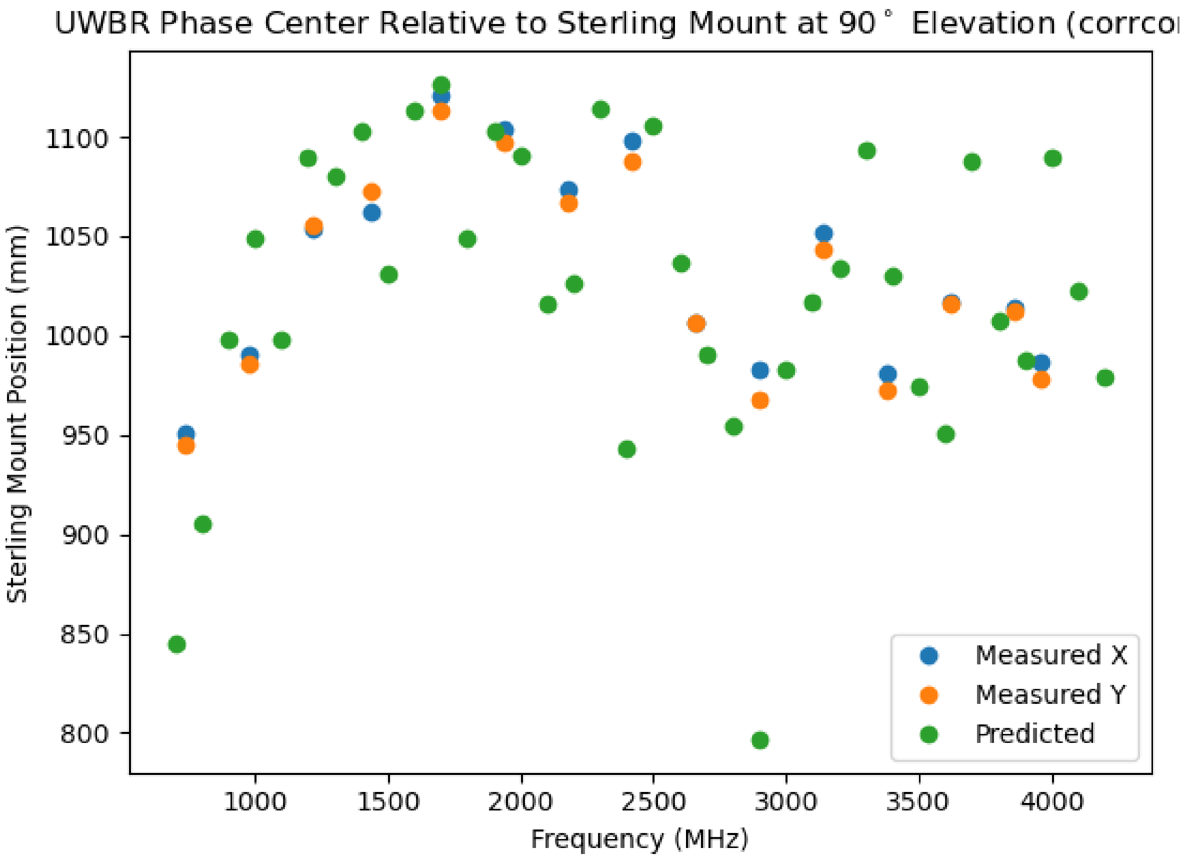

Figure 21: Derived phase center of UWBR for the X and Y polarization channels as a function of frequency. Model predictions are also shown. See text for details.

focus offset to the current focus tracking model at the observed elevation.

2. Because observations are taken over a range of elevations, the results of step 1) must be referenced to a common elevation. For this step we used the new focus tracking model that we derived in §11.
3. The results of step 2) must be converted to a distance from a reference plane that is located at the probe at the bottom of the UWBR feedhorn. This reference frame is 300.1416 mm from the Sterling mount mounting plate. We also must add 508 mm to account for the 20-in extension drum that attached to the front-end box.

Fig. 21 shows the measured phase center as a function of frequency for the X and Y polarization, as well as the predicted phase center according to models of the feed. The data typically agree with the model to within ±50 mm, and we see broadly similar trends.

We attempted to measure the lateral phase center as a function of a frequency by following the same routine as in §11.2, but adjusting the frequency used for cross-elevation scans rather than observing over a wide range of elevations. However, we were unable to obtain good fits to the optimal lateral focus offset as a function of frequency.

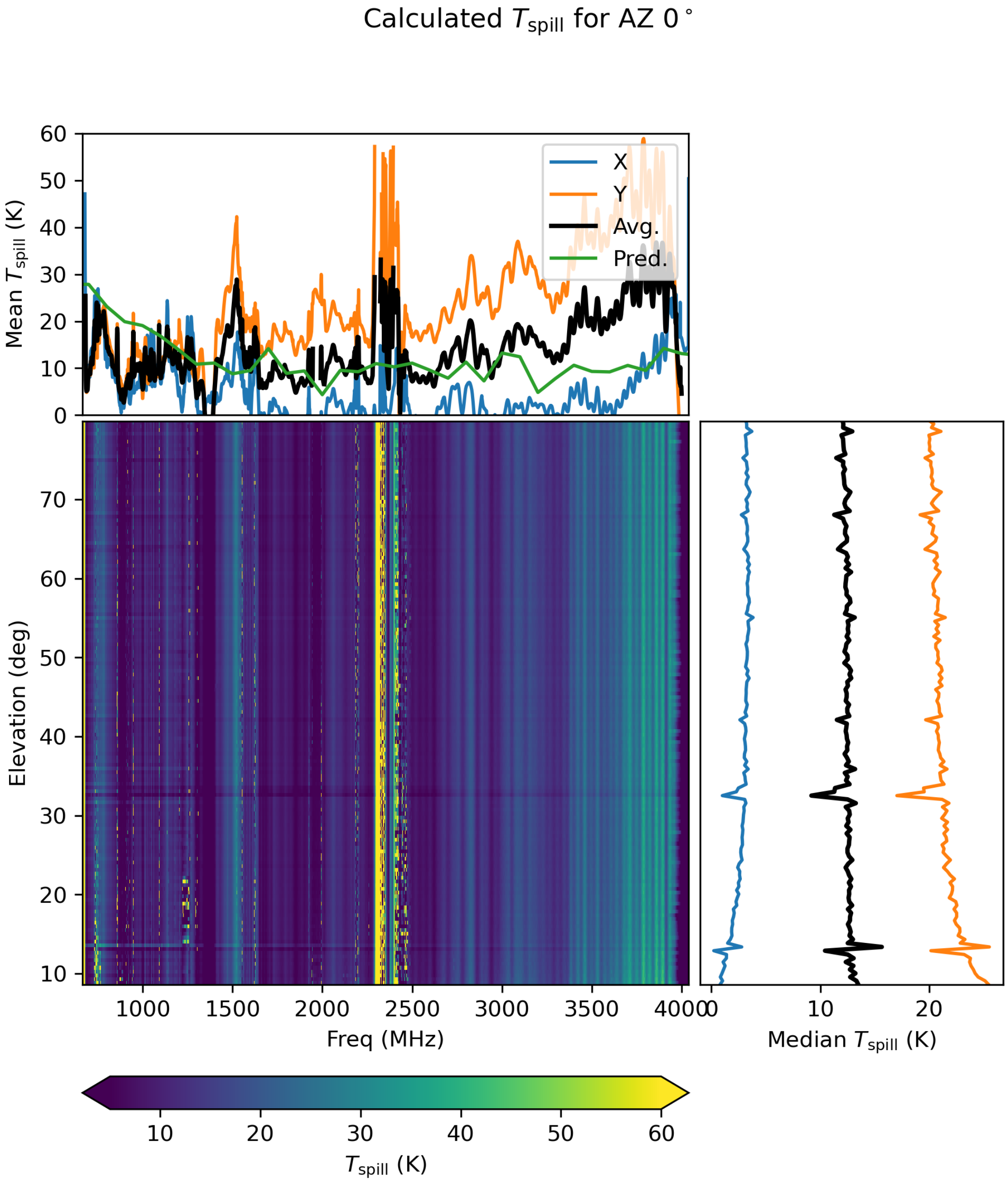

Figure 22: Derived $T_{\rm spill}$ as a function of frequency and elevation at 0° azimuth. As noted in the text, the derived values agree with predictions below 3 GHz when considering the average of the two polarization channels, but when analyzing each channel independently the derived values are lower/higher than expected in X/Y, respectively. The reason for this is unclear.

13 Spillover Measurement

We followed the formalism of Maddalena et al. (2012) in an attempt to measure UWBR's spillover temperature as a function of frequency and elevation. These authors define the spillover efficiency as a function of airmass as

$$\eta_{\rm spill}(A) = \frac{(T_{\rm cmb} + T_{\rm gal} - T_{\rm atm})\, e^{-\tau A} + T_{\rm atm} + T_{\rm rcvr} - T_{\rm sys}(A)}{(T_{\rm cmb} + T_{\rm gal} - T_{\rm atm})\, e^{-\tau A} + T_{\rm atm} - T_{\rm ground}} \tag{9}$$

where $A = \csc(E)$ and E is elevation. The spillover temperature is then $T_{\rm spill} = \eta_{\rm spill} T_{\rm ground}$. We performed tipping observations using VEGAS in Mode 1 at azimuths of 0–315° in 45° increments and calculated the spillover temperature as a function of frequency and elevation. We assumed $T_{\rm atm} = T_{\rm ground} = T_{\rm amb}$ where $T_{\rm amb}$ is the ambient temperature at the time of the observation and also assumed $\tau = -0.008$. The results for a representative azimuth are shown in Fig. 22, along with the predicted $T_{\rm spill}$ from modeling of the feed patterns. The results are interesting. When averaging the two polarizations the derived and predicted $T_{\rm spill}$ are in close agreement at frequencies < 3 GHz, but above 3 GHz the derived $T_{\rm spill}$ is higher than expected. The most significant deviations of the SEFD and $T_{\rm sys}$ from the target values also occur at > 3 GHz (see Fig. 4). Higher than expected $T_{\rm spill}$ is thus a likely reason for this excess noise. We note that $T_{\rm spill}$ does not show any dependence on elevation or azimuth.

However, when examining the two polarizations independently $T_{\rm spill}$ deviates from the model significantly. In fact, the derived $T_{\rm spill}$ in the X polarization takes on nonphysical values (i.e. < 0 K) at some frequencies. The reason seems to be that $T_{\rm sys}$ is higher than expected in the Y channel but lower in the X channel, but we are unable to explain why this is the case. We see no such discrepancy in other $T_{\rm sys}$ measurements (see §3 and 3.2), nor do we see any sign that the $T_{\rm cal}$ values that we used to derive $T_{\rm sys}$ are in error (see §3.2). We used the same data reduction approach to calculate $T_{\rm sys}$ as described elsewhere in this report. It may be useful to repeat these observations in the future to see if the discrepant values in each polarization channels persist. However, this discrepancy does not prevent scientific use of the receiver.

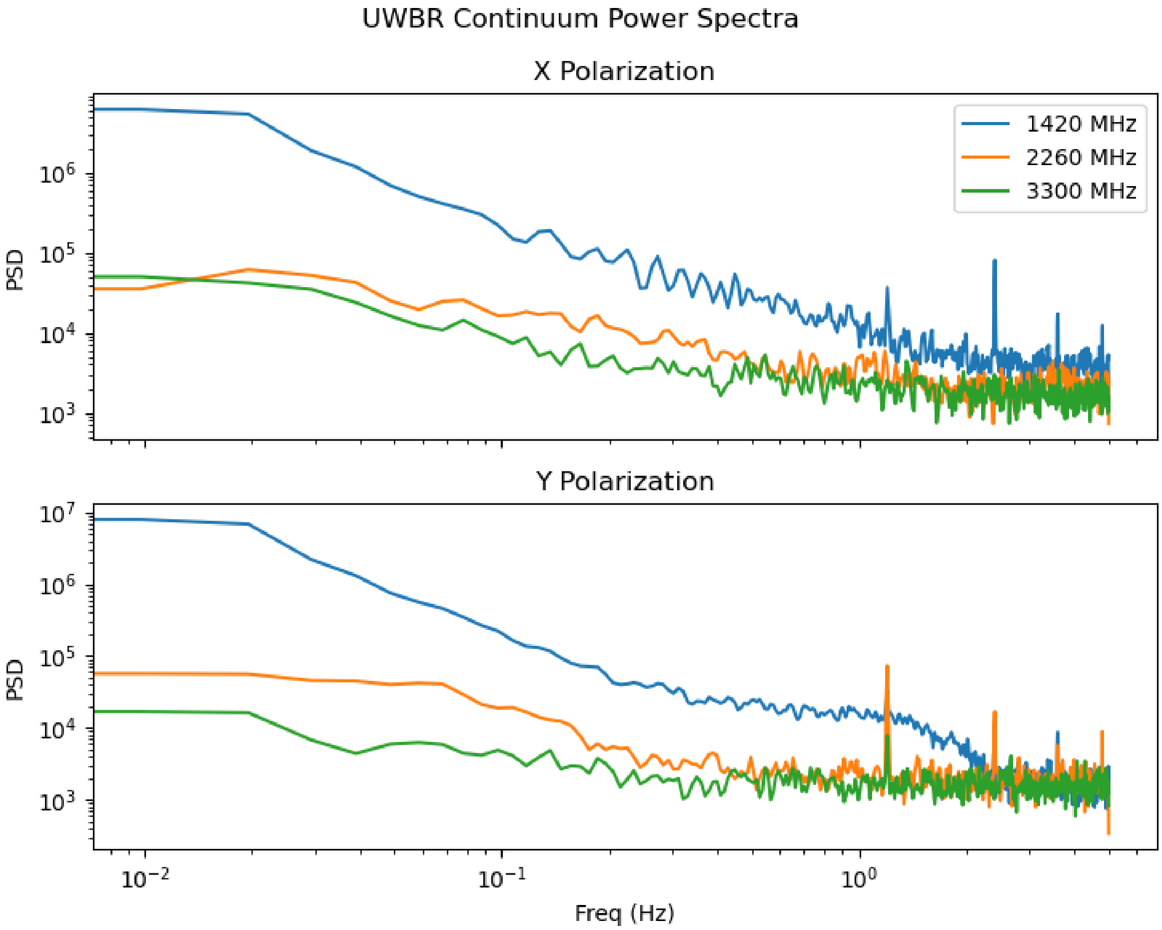

Figure 23: UWBR PSD obtained using the DCR with 80 MHz bandwidth at three different frequencies.

14 $1/f$ Noise Measurement

To characterize $1/f$ noise we observed the North Celestial Pole using the DCR at three frequencies: 1420, 2660, and 3300 MHz, each with a bandwidth of 80 MHz. The sampling time was 0.1 seconds and the total scan length of each scan was 900 seconds. Our observation at 2660 MHz was impacted by what we believe to be strong RFI – approximately 70 seconds into the scan we observe a dramatic increase in power, followed by a drop below the previous mean power and a slow recovery. To avoid this, we only used data after the first 100 seconds of the scan at 2660 MHz.

We then computed the power spectral density (PSD) of each observation using Welch's method and plotted the resulting PSDs in logarithmic space (see Fig. 23). The $1/f$ noise limit should manifest as a "knee" in the spectrum where the slope of the PSD transitions from zero (i.e. white noise) to approximately -1. At 1420 MHz the knee frequency appears to be around 2.5 Hz. At 2260 and 3300 MHz the upturn is less dramatic and appears to be around 0.8 Hz.

15 Conclusion

We performed a wide range of scientific commissioning observations with UWBR, demonstrating its scientific potential for the study of pulsars (and by extensions other fast transients) and the ISM in molecular emission. UWBR's wide bandwidth will benefit high precision pulsar timing projects and wideband study of pulsars and FRBs in general, and it opens a new 3–4 GHz window on the GBT. We performed a number of technical and utility observations to measure SEFD, T_{sys}, and gain; measure the polarimetric properties of the receiver; determine the optimal focusing frequency; measure the beam shape; derive a new focus tracking model; verify laboratory-measured T_{cal} values; measure the phase center and compare it with laboratory-derived values; characterize the spillover efficiency; and measure the $1/f$ noise. We recommend releasing the receiver for scientific use, and also recommend a few post commissioning activities that were either beyond the scope of this report or are worth repeating to improve on the results presented here:

- UWBR should be used to derive a new prime focus pointing model.
- Mueller Matrix observations should be repeated with full symmetric hour angle coverage.
- T_{spill} measurements should be repeated to investigate the high/low T_{spill} in the individual Y/X polarization data, respectively.

Overall the receiver is performing well and we look forward to it enabling new science using the GBT.

Acknowledgments

UWBR was funded in part by the Gordon and Betty Moore Foundation through grant GBMF7576 to Associated Universities, Inc. to support the work of the Green Bank Observatory and NANOGrav Physics Frontiers Center. The National Radio Astronomy Observatory and Green Bank Observatory are facilities of the U.S. National Science Foundation operated under cooperative agreement by Associated Universities, Inc.

References

Alam, Md F. et al. (Jan. 2021). "The NANOGrav 12.5 yr Data Set: Observations and Narrowband Timing of 47 Millisecond Pulsars". In: ApJS 252.1, 4, p. 4. DOI: `10.3847/1538-4365/abc6a0`. arXiv: `2005.06490 [astro-ph.HE]`.

Balser, Dana S. et al. (Aug. 2001). "GBT Prime Focus (Band 1-4): Focus Tracking". In: *GBT Commissioning Memo* 12, pp. 1–10.

Britton, M. C. (Apr. 2000). “Radio Astronomical Polarimetry and the Lorentz Group”. In: ApJ 532.2, pp. 1240–1244. DOI: `10.1086/308595`. arXiv: `astro-ph/9911101 [astro-ph]`.

Cohen, T. (2025). Private communication.

Dai, S. et al. (May 2015). “A study of multifrequency polarization pulse profiles of millisecond pulsars”. In: MNRAS 449.3, pp. 3223–3262. DOI: `10.1093/mnras/stv508`. arXiv: `1503.01841 [astro-ph.GA]`.

Haslam, C. G. T. et al. (Jan. 1982). “A 408-MHZ All-Sky Continuum Survey. II. The Atlas of Contour Maps”. In: A&AS 47, p. 1.

Jacob, Arshia M. et al. (Dec. 2024). “Revisiting rotationally excited CH at radio wavelengths: A case study towards W51”. In: A&A 692, A164, A164. DOI: `10.1051/0004-6361/202449603`. arXiv: `2411.08193 [astro-ph.GA]`.

Lam, M. (2025). Private communication.

Lam, M. T. et al. (July 2018). “Optimal Frequency Ranges for Submicrosecond Precision Pulsar Timing”. In: ApJ 861.1, 12, p. 12. DOI: `10.3847/1538-4357/aac48d`. arXiv: `1710.02272 [astro-ph.HE]`.

Maddalena, Ronald J. et al. (Jan. 2012). “Accurately Measuring the Spillover of a Radio Telescope”. In: *American Astronomical Society Meeting Abstracts #219*. Vol. 219. American Astronomical Society Meeting Abstracts, 422.38, p. 422.38.

Manchester, R. N. et al. (Apr. 2005). “The Australia Telescope National Facility Pulsar Catalogue”. In: AJ 129.4, pp. 1993–2006. DOI: `10.1086/428488`. arXiv: `astro-ph/0412641 [astro-ph]`.

Perley, R. A. et al. (May 2017). “An Accurate Flux Density Scale from 50 MHz to 50 GHz”. In: ApJS 230.1, 7, p. 7. DOI: `10.3847/1538-4365/aa6df9`. arXiv: `1609.05940 [astro-ph.IM]`.

Price, Danny C. (Mar. 2016). *PyGDSM: Python interface to Global Diffuse Sky Models*. Astrophysics Source Code Library, record ascl:1603.013. ascl: `1603.013`.

van Straten, W. et al. (Mar. 2010). “PSRCHIVE and PSRFITS: Definition of the Stokes Parameters and Instrumental Basis Conventions”. In: PASA 27.1, pp. 104–119. DOI: `10.1071/AS09084`. arXiv: `0912.1662 [astro-ph.IM]`.

Zhang, Xi-Zhen et al. (Sept. 2012). “New radio observations of the Moon at L band”. In: *Research in Astronomy and Astrophysics* 12.9, pp. 1297–1312. DOI: `10.1088/1674-4527/12/9/010`.